

ACCELERATED SIMULATION OF SUPERCAPACITORS USING ORDER REDUCTION
TECHNIQUES AND WAVEFORM RELAXATION METHODS

by

FATIH CINGOZ

Presented to the Faculty of the Graduate School of
The University of Texas at Arlington in Partial Fulfillment
of the Requirements
for the Degree of

MASTER OF SCIENCE IN ELECTRICAL ENGINEERING

THE UNIVERSITY OF TEXAS AT ARLINGTON

May 2012

Copyright © by Fatih Cingoz 2012

All Rights Reserved

ACKNOWLEDGEMENTS

First of all, I want to express my sincere gratitude to my advisor, Dr. Ali Davoudi, for providing a great opportunity to work. During my research, Dr. Davoudi always encouraged me to improve my research skills together with invaluable guidance and advice.

I would like to also thank the Ministry of National Education of Turkey for their financial support throughout my graduate studies. Further, I would like to thank professors Dr. Sungyong Jung and Dr. Rasool Kenarangui for allowing time to serve on my thesis committee and my colleagues at the Renewable Energy and Vehicular Technology Laboratory for their insights, comments, discussions and ideas. In addition, I want to thank Pulsed power group for letting me use Metrohm Autolab PGSAT 302N.

Special thanks to my fiancée for her encouragement and priceless support during my hard times. In addition, I also want to express thanks to my parents, who endured my absence during my studies. Last, I thank Ms. Amy Tuttle for helping me with the script corrections of my thesis.

May 12, 2012

ABSTRACT

ACCELERATED SIMULATION OF SUPERCAPACITORS USING ORDER REDUCTION TECHNIQUES AND WAVEFORM RELAXATION METHODS

FATIH CINGOZ, MS

The University of Texas at Arlington, 2011

Supervising Professor: Dr. Ali Davoudi

Supercapacitors are promising energy storage devices due to their capability to deliver high peak current and to capture a huge amount of energy in a short time with very low internal power loss. They are candidate component to be used in as a secondary energy storage device in hybrid electric vehicles (HEV)). Precise model development and accelerated simulation environments are needed to minimize the design time (and subsequently the product-to-market time) and minimize the hardware redesign and retrofit.

Transmission line and RC parallel-branch equivalent models show relatively higher accuracy in predicting the dynamic behavior of the device. They also have shown features such as easy parameter identification from experimental data and easy adaptation to other system simulation tools. However, these circuit models have higher order compared to the other existing equivalent circuit model, and are computationally intensive.

This thesis provides an extensive characterization analysis for a commercialized supercapacitor by means of electrochemical impedance spectroscopy (EIS). Based on the EIS measurements, the circuit parameters for both circuit models (RC parallel-branch and transmission line models) have been extracted and validated. First, the performance of the

order reduction techniques, when applied to high-order RC parallel-branch models, has been investigated. It has been shown that the high-order RC parallel-branch models, which show high accuracy in dynamic behavior of the supercapacitor, can be effectively reduced to low order models. The reduced-order models can be computed faster without compromising the model accuracy. Then, the features of the transmission line model of supercapacitor have been exploited by one of the waveform relaxation methods, which is an iterative method used for solving differential equations, in order to obtain fast time-domain simulation of supercapacitor. These aforementioned studies have been performed using numerical simulation and hardware measurement.

TABLE OF CONTENTS

ACKNOWLEDGEMENTS.....	iii
ABSTRACT.....	iv
LIST OF ILLUSTRATIONS.....	viii
LIST OF TABLES	x
Chapter	Page
1. INTRODUCTION.....	1
1.1 Background and Discussion.....	1
1.2 Motivation and Objective	4
1.3 Thesis Outline.....	5
2. OVERVIEW OF SUPERCAPACITORS	6
2.1 Description of Supercapacitors	6
2.2 History of Supercapacitors	7
2.3 Principles of Supercapacitors	9
2.4 Structure of Supercapacitors	12
2.4.1 Electrode materials.....	13
2.4.2 Electrolytes	14
2.4.3 Separator.....	15
3. SUPERCAPACITOR CHARACTERIZATION AND MODELING	16
3.1 Characterization of Supercapacitor	16
3.1.1 Electrochemical Impedance Spectroscopy	16
3.1.2 Analysis of Impedance Spectroscopy Measurements	18
3.1.3 Voltage and Thermal dependence	20
3.2 Modeling of Supercapacitor.....	23

3.2.1 Overview of existing equivalent circuit models.....	23
3.2.2 Porous Impedance Theory	25
3.2.2.1 Transmission Line Model of Pore Impedance	28
3.2.2.2 RC parallel-branch Model of Pore Impedance	29
4. REDUCED ORDER ANALYSIS OF HIGH-FIDELITY RC PARALLEL-BRANCH MODEL OF SUPERCAPACITOR	31
4.1 Order Reduction Theory	31
4.2 Analysis of High-fidelity RC Parallel-branch Model	32
4.3 Order Reduction Framework	36
4.4 Balanced Order Reduction	37
4.5 Krylov-subspace Method	39
4.6 Case Studies	41
5. ACCELERATED SIMULATION OF SUPERCAPACITOR USING WAVEFORM RELAXATION	45
5.1 Waveform Relaxation Theory	45
5.2 Analysis of Transmission Line Model (TLM)	49
5.3 Discussion of Waveform Relaxation Techniques	51
5.3.1 Circuit Partitioning and relaxation process	51
5.3.2 Time Windowing and Scheduling	57
5.4 Experimental Setup and Simulation Results	59
6. CONCLUSIONS	63
APPENDIX	
A. SUPERCAPACITOR DATA SHEET	65
B. CIRCUIT PARAMETERS.....	67
REFERENCES	69
BIOGRAPHICAL INFORMATION	78

LIST OF ILLUSTRATIONS

Figure	Page
1.1 Sample of electric power architecture in HEVs	2
2.1 The Ragone plot of different energy storage devices.....	7
2.2 The supercapacitors produced by (a) GEC and (b) SOHIO	8
2.3 A range of supercapacitor cells and modules sold by Maxwell Company.....	8
2.4 Simplified structure of electrostatic capacitor	9
2.5 Simplified cation accumulation on the negatively charged electrode [19].....	11
2.6 The basic structure of the supercapacitor modified from [19]	13
3.1 Test bench overview: (a) Metrohm Autolab PGSTAT 302N (b) Current booster (c) Maxwell BCAP2000 supercapacitor (d) laser thermometer	17
3.2 Imaginary and real part of supercapacitor impedance as a function of frequency with bias voltage of 2.5 V and a temperature of 22 °C	18
3.3 The imaginary part of supercapacitor impedance for different bias voltages vs. frequency	20
3.4 The supercapacitor capacitance as a function of voltage at 22 °C	21
3.5 Measurement of the supercapacitor resistance at various bias voltages of 0.002, 0.5, 1, 1.5, 2.0 and 2.5V and a temperature of 22°C.....	22
3.6 The supercapacitor theoretical model	24
3.7 The supercapacitor classical RC model	24
3.8 Three-branch equivalent circuit model of supercapacitor developed by Zubeta and Bonert	25
3.9 A small structure of supercapacitor (b) 3-D visualization of ideal porous electrode(modified from [19]) (c) Distributed model of a single pore.....	26
3.10 The equivalent circuit model based on the Porous Electrode Theory	28
3.11 The transmission line model of pore impedance	29
3.12 The RC parallel-branch model of pore impedance	29

4.1	High-fidelity RC parallel-branch model of supercapacitor	32
4.2	The Nyquist plot of the measured impedance of 2 kF supercapacitor at 2.5 V , 22 °C	33
4.3	The bode plot of measured impedance and high-fidelity model impedance at 2.5 V , 22 °C	34
4.4	Block diagram of model order reduction process	35
4.5	Frequency response of the supercapacitor impedance in 60 th and 4 th order models extracted by SPA method	42
4.6	Frequency response of the supercapacitor impedance in 60 th and 4 th order models extracted by TBR method	42
4.7	Frequency response of the supercapacitor impedance in 60 th and 4 th order models extracted by Krylov-subspace method	43
4.8	Frequency response of the supercapacitor impedance in 60 th and 4 th order models extracted by: SPA , TBR, and Krylov-subspace methods	43
4.9	Frequency response of the supercapacitor impedance in 60 th , 4 th models and reduced 4 th order model (by SPA method)	44
5.1	Circuit simulation procedure using Gauss-Jacobi waveform relaxation method	47
5.2	Five-stage TLM of supercapacitor	50
5.3	Frequency responses of the measured impedance of supercapacitor and the impedance predicted by TLM.	50
5.4	Circuit interpretation of GJ-WR applied to the circuit shown in Figure 5.2	54
5.5	The illustration of simulation process of (a) implemented WR method and (b) conventional method	58
5.6	The experimental setup: (a) Lecroy 640Zi oscilloscope, (b) Sorensen DCS40-75E DC power supply, (c) supercapacitor (Maxwell Boostcap), (d) Lecroy CP150 current probe, (e) Lecroy voltage probe	60
5.7	The experimental current and voltage measurement	61
5.8	Simulation results of transient response of investigated supercapacitor using WR and conventional methods	62

LIST OF TABLES

Table	Page
1.1 Comparisons of supercapacitors and batteries	3
2.1 Current companies manufacturing supercapacitors	9

CHAPTER 1

INTRODUCTION

1.1 Background and Discussion

In contrast to the conventional vehicles, Hybrid Electric Vehicles (HEVs) have more electrical components such as AC motors, DC/AC power converters, embedded supervisory controllers, Energy Storage Units (ESU), etc. Among these, ESU requires deep consideration in the design procedure since it plays a key role in providing sufficient energy and power to sustain normal operation of the vehicle. This unit usually consists of fuel cell stacks, batteries, and supercapacitors. The ESU used in HEVs is basically expected to densely supply and absorb energy in the sudden accelerating and regenerative braking instants, respectively. This expectation, if satisfied, can significantly improve the vehicle performance. In order to design such an ESU, a better understanding of the system requirements and dynamics during a test drive is crucial. Due to the sophisticated dynamic interactions among the electric components and the need of having interdisciplinary knowledge (interaction of mechanical and electric components), a suitable ESU design offers a challenging procedure. Furthermore, prototyping the whole system including supervisory controllers, converters and electric machines to test an ESU is difficult, costly, and time consuming. Therefore, modeling and simulation before prototyping and assembling are necessary steps toward optimizing the ESUs for size and weight.

The ESU is expected to provide instantaneous high power and also sufficient energy with a long lifespan and long lifecycle in HEV applications. It also needs to be charged fast enough to store as much energy as possible during regenerative braking. Since batteries are low cost and high energy dense, they are typically used in ESU as a primary energy storage device.

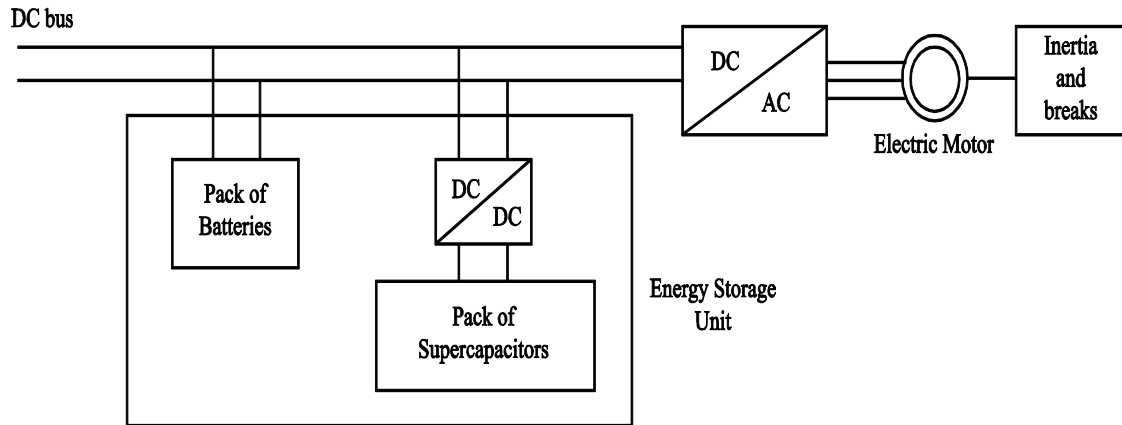


Figure 1.1 Sample of electric power architecture in HEVs.

However, the short lifecycle, slow charge and discharge rate, and low current capacity of the batteries limit their applications in HEV. These drawbacks have been recently alleviated by adding supercapacitors in ESU as shown in Figure 1.1. Compared to a battery, a supercapacitor has a longer lifecycle, higher efficiency, faster charging and discharging rate, and wider operating temperature range. Due to the fast charging rate of supercapacitors, the vehicle kinetic energy can be sufficiently absorbed and stored. Furthermore, since supercapacitors have much higher power density than batteries, they also can meet the high instantaneous power demand during acceleration while the batteries can usually provide power for the constant speed vehicle operation. This duty sharing strategy lengthens the lifespan of the battery and improves the vehicle performance [1], and at the same time it increases reliability of the ESU [2]. Table 1.1 gives a detailed comparison of batteries and supercapacitors.

Table 1.1 Comparisons of supercapacitors and batteries [3]

	Battery	Super-capacitor
Power Density	50-200 W/kg	1000-2000 W/kg
Energy Density	20-100 Wh/kg	1-10 Wh/kg
Discharge Time	0.3-3 hrs	1-30 sec
Charge Time	1-5 hrs	1-30 sec
Lifecycle	500-2000	>500.000
Efficiency	70-85%	90-95%
Operating Temp.	0 °C – 60 °C	-40 °C – 70 °C
Safety	Good	Good
Maintenance	Good	Very Good

Although battery and supercapacitor combination proposes remarkable advantages, it raises new challenges in the ESU design procedure including:

- A proper control strategy is required to split the flow of power between the battery and the supercapacitor, and thus to effectively improving the battery life.
- During charging and discharging stages, dynamic responses of both storage components need to be precisely investigated.
- Size and weight of the storage components should be optimized in order to reduce the overall cost.

ESU designers utilize simulators, such as ADvanced VehIcle SimulatOR (ADVISOR), Virtual Test Bed (VTB), and Power-train System Analysis, to overcome these aforementioned challenges. These simulation tools particularly allow users to observe and explore dynamic response of a complex interdisciplinary system with the help of incorporated circuit-based models used in the virtual modules [4]-[6]. Designers investigate the optimal control strategy for the ESU by observing the dynamic response of the storage devices at various urban driving maneuvers. As a result, the power controller, which is in charge of sharing the energy and power between the battery and supercapacitor, can be efficiently designed. Moreover, optimal values for battery and supercapacitor and the voltage leveling converters, connecting storage devices to

the internal DC bus (see Figure 1.1), can be designed easily to meet the power and energy requirements [7]. Therefore, one must notice that the optimal ESU design can be achieved when a precise battery and supercapacitor model is incorporated in the simulators. Due to the demand for precise equivalent circuit models, several models for supercapacitor and battery have been proposed [8]-[13].

1.2 Motivation and Objective

The current profiles applied to supercapacitors in HEV applications comprise frequent charge and discharge pulses as investigated in [14] and [15]. During normal operation of a HEV, the supercapacitor bank repeatedly supplies charging and discharging current pulses in accordance to vehicle speed profile, which typically consists of stop-and-go micro-cycles [15]. This indicates that the supercapacitor covers much faster dynamics than the battery, and thus, this thesis has focused on equivalent circuit models for supercapacitor which can precisely model dynamic behavior of this component.

Different models have been proposed for supercapacitor namely: classical RC model, three branch model, transmission line model, and RC parallel-branch model. Each model has its own advantages and disadvantages according to the specific operational considerations. The classical RC model of a supercapacitor is not feasible for characterizing the supercapacitor in a wide range of frequencies [12]. Three-branch model [13] shows good accuracy in a time range of 30 minutes, but it is not appropriate for transient simulations since the parameters of the model are calculated through constant current tests [16]. RC parallel-branch model [18] and transmission line model alleviate the problems of the former models and is the best choice as far as simulating the dynamic behavior of supercapacitor is concerned. These models show high-order properties due to their higher number of passive components. Accordingly, these models are computationally inefficient in simulations. Computational efficiency in ESU analysis is of concern since the design procedure is based on trial and error, and the users need to execute the models several times. Therefore, even a small improvement in simulation time is highly

desired by the designers. From general perspective, analysis of large supercapacitor packs requires highly efficient computational methods that also provide high accuracy.

In this research, since better understanding of the equivalent circuit models requires extensive knowledge of the electrical features of supercapacitors, this work first investigates fundamentals and the frequency analysis of supercapacitors. Subsequently, the model order reduction technique is used to extract the low-order dynamic model of supercapacitors from the high-order RC parallel-branch model. In other words, the original high-order state-space model has been replaced by a low-order state-space model through the order reduction process. This process almost preserves the input-output relationship. The reduced order model shows an acceptable accuracy while significantly reducing the computational time in simulations. Second, this thesis also focuses on the waveform relaxation (WR) method to be applied to the transmission line model of supercapacitor. Computational speed-ups in simulations are obtained by developing algorithms for WR techniques, namely: circuit partitioning, time windowing, and scheduling. In general, the objective is to accelerate the execution procedure of the investigated models while the accuracy is kept within acceptable levels.

1.3 Thesis Outline

The rest of the thesis is organized as follows: Chapter 2 reviews the physical and electrochemical basics of supercapacitor technologies. In Chapter 3, first, electrochemical impedance spectroscopy (EIS) is used to characterize the input impedance of a commercialized supercapacitor within a wide range of frequency for different bias voltages. Then, based on the measured impedance, the existing equivalent circuit models will be extracted. In Chapter 4, the model order reduction techniques are discussed and applied to the validated high-order RC parallel-branch model. The Chapter 5 focuses on the accelerated simulation of the validated transmission line model using the waveform relaxation method. Finally, Chapter 6 provides the conclusions of this research and future directions.

CHAPTER 2

OVERVIEW OF SUPERCAPACITORS

2.1 Description of Supercapacitors

For over a century, conventional capacitors have been only employed in low power applications such as memory backup supplies or analogue circuits due to their low capacitance. However, manufacturers have produced materials featuring high surface-area and low resistance. As a result, a unique energy storage device that capable of storing relatively higher energy in the form of electrical charge has been produced. Over the years, this storage device has been named by many manufacturers, which are: supercapacitors, dynacaps, gold capacitors, and electrochemical double layer capacitors [18], [19]. Throughout this thesis the term ‘supercapacitors’, which is mostly used trade name and settled by Nippon Electric Company (NEC), will be used.

Supercapacitors are constructed of high surface electrode materials (e.g., activated carbon), and thin electrolytic dielectrics in order to boost up the capacitance value. As a result, supercapacitors show the ability to store larger amount of energy than conventional capacitors, while still preserving high power density characteristics of conventional capacitors. The Ragone plot, which represents a device’s energy and power capabilities, depicted in Figure 2.1, shows the most recent position of supercapacitor among the other storage devices. Compared with batteries, supercapacitors have longer lifecycle, higher efficiency, faster charge/discharge capability, and wider operating temperature range. Therefore, they have received a significant attention by many researchers for to be utilized in a variety of potential applications such as memory backup, quick charge, battery life improvement, and uninterruptable power supplies [20]. Recently, they are also used in a wide range of high-power applications such as advanced

transportation (e.g. HEVs, buses, and power-trains) and electric utility applications (e.g. stabilization, voltage regulation, and power factor correction of transmission lines) [21].

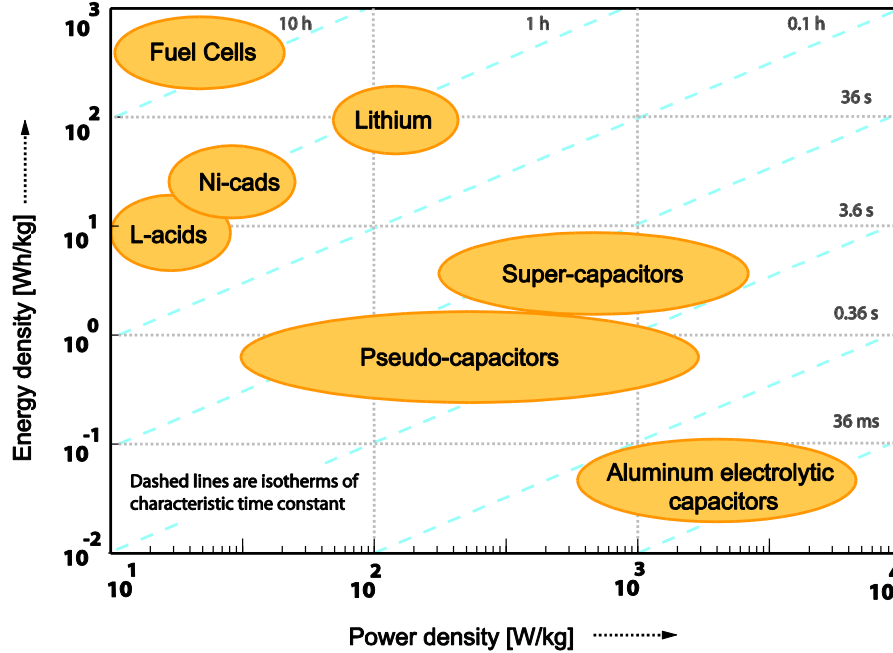


Figure 2.1 The Ragone plot of different energy storage devices [20]

2.2 History of Supercapacitors

The practical utilization of supercapacitors was first introduced in 1957, when General Electric Company (GEC) developed the first patented supercapacitor. As shown in Figure 2.2 (a), it is made of porous carbon electrodes modified based on a double-layer capacitance mechanism for electric charge [19]. Another patent for supercapacitor was placed by the Standard Oil Company (SOHIO) for practical applications in 1966. Figure 2.2 (b) illustrates the structure of supercapacitor patented by SOHIO. This company became unsuccessful in the commercialization of their invention and thus licensed the technology to NEC. In the following years, advanced supercapacitors featuring high internal resistance were produced by NEC and employed mostly in memory backup applications [18]. In 1978, the same company marketed the first supercapacitor products used as memory backup in computers. The manufacturing of supercapacitors accelerated after 1980, and many companies listed in the Table 2.1 [22] have

begun to market their products in various sizes and types. As an example of commercial supercapacitor, Figure 2.3 shows supercapacitors named 'boostcap' which is manufactured by Maxwell Company in USA.

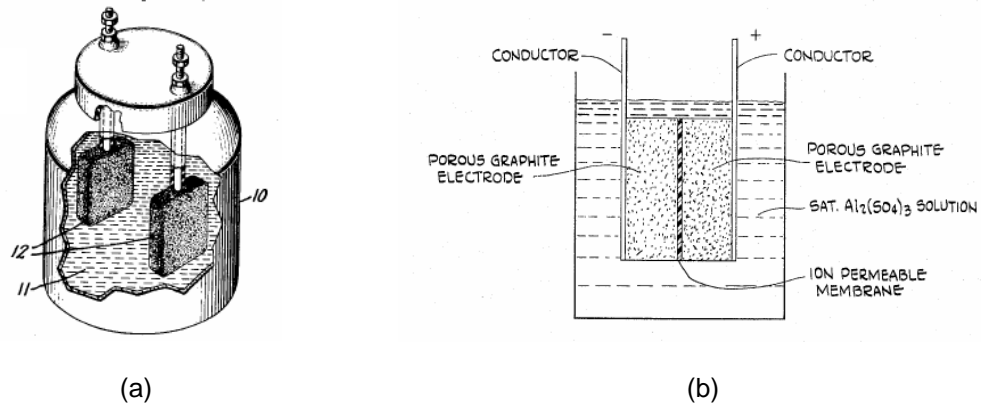


Figure 2.2 The supercapacitors produced by (a) GEC [23] and (b) SOHIO [24]



Figure 2.3 A range of supercapacitor cells and modules sold by Maxwell Company [25]

Table 2.1 Current companies manufacturing supercapacitors

Company	Country	Energy Storage and DC Voltage Ratings	VDC /Cell
ECOND	Russia	40 kJ, 14 - 200 V modules	0.9
Elit Stock Company	Russia	50 kJ, 14 - 400 V	9
EPCOS AG	Germany	15 kJ, 2.5 V – 40kJ, 14 V	2.5-2.7
ESMA Joint Stock Company	Russia	20 kJ – 1.2 MJ, 14 V 30 MJ, 180 V modules	1.4-1.6
Maxwell Technologies Inc.	USA	8 kJ, 2.5 V	2.3-2.5
NESS Capacitor Company	Korea	18 kJ, 2.7 V	2.5 – 2.7
NEC Tokin	Japan	8 kJ, 14 V	0.9
Okamura Laboratory Inc.	Japan	1350 – 1500 F, 2.7 V 35 F, 346 V, 75 F, 54 V	2.5 – 2.7
Panasonic	Japan	6 kJ, 2.5 V	2.5 – 2.7
Saft	France	10 kJ, 2.5 V	2.5 – 2.7

2.3 Principles of Supercapacitors

Due to the operation similarity of conventional capacitors and supercapacitors, in this section the operation principles of electrostatic capacitors will be briefly reviewed. Basically, electrostatic capacitors are made of two parallel metal electrodes (also known as conducting plates) separated by a dielectric (e.g., air, paper, polyester, oxide, vacuum, etc), as shown in Figure 2.4.

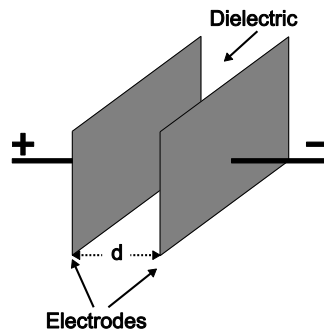


Figure 2.4 Simplified structure of electrostatic capacitor

Once the capacitor is subjected to an electric potential across the electrodes, electrons start flowing and an electrical charge accumulates on both the positive and negative electrodes. In case of removing the potential, the energy is discharged only if there is a physical connection between the conducting plates, otherwise the capacitor remains charged [26].

The strength of dielectric, measured in volts per meter, plays a crucial role in determining the operating voltage of the capacitor. The strength of dielectric is determined by achievable maximum electric field without dielectric breakdown [26]. The dielectric strength depends upon the thickness and type of the material. High dielectric strength is always desired in order to achieve high capacitance value and maximum operating voltage of the capacitor. The capacitance value of the capacitor and stored energy is defined by the following equations:

$$C = \frac{Q}{V} = \varepsilon \frac{A}{d} \quad (2.1)$$

$$E = \frac{1}{2} CV^2 = \frac{1}{2} QV \quad (2.2)$$

where C is capacitance in Farads, Q is the charge in Coulombs, V is electric potential in Volts across the conductors, ε is the dielectric constant, A is the surface area of the electrode, and d is the distance between electrodes. The power of the capacitor is given by

$$P = \frac{V^2}{4R} \quad (2.3)$$

where the R is the internal resistance.

Supercapacitors accumulate the electrical charge inside the surface of electrode material soaked in the electrolytic solution. Since the supercapacitors are constructed of two electrodes separated by a porous membrane, an electrical layer is formed at each electrode-electrolyte interface by the stored charge. This electric charge separation leads to the electric double-layer present. In 1853, Helmholtz first described the electric double-layer model to study the capacitive properties of electrode/electrolyte interface. According to the model, each electrode/electrolyte interface consists of two monolayers, in which one forms on the positively or negatively charged electrode while the other is comprised of ions in the electrolyte [20]. With

the presence of the electric potential across current collectors, electrons begin to flow and accumulate on the negative electrode, which attracts the cations (positive ions) into the electrode surface to balance the charge. In the same way, the anions (negative ions) are attracted by the electron vacancies on the positive electrodes into the electrode surface to balance the charge. The division of accumulated ionic and electronic charge is the origin of the term 'double-layer' capacitor. Double-layer capacitance forming on both negative and positive electrodes is added in series to the total of capacitance of the supercapacitor [19]. A simplified cation accumulation on the electrode surface is illustrated in Figure 2.5.

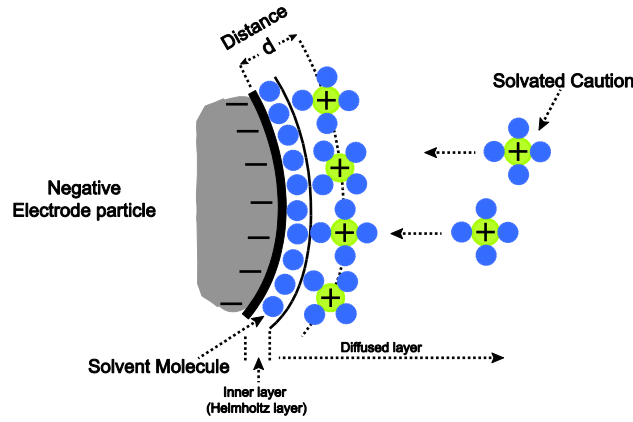


Figure 2.5 Simplified cation accumulation on the negatively charged electrode [19]

When the electrical potential is applied across the current collectors, two layers are formed as the inner and outer layers, as shown in Figure 2.5. The inner layer (Helmholtz layer) is essentially made of non-conductive solvent molecules; the outer layer (diffused layer) is mainly made of solvated ions that are surrounded by the solvent molecules [27]. The separation d between the ions and the polarized electrodes is in the order of a few angstroms. The differential capacitance modeled by Helmholtz can be written as

$$C_H = \frac{A\varepsilon}{4\pi d} \quad (2.4)$$

where C is the capacitance, A is the surface area, ε is the relative dielectric constant, and d is the thickness of the double layer. Helmholtz double-layer method has been found to be insufficient to model the double layer capacitance because it does not take the voltage and

temperature dependency of the capacitance into account. In 1900, another double-layer model was developed by Gouy and Chapman. Basically, these researchers have studied the capacitance dependency on the operating voltage and ionic concentration. The differential of Gouy-Chapman capacitance is described by

$$C_{GC} = AZF \sqrt{\frac{2c\varepsilon}{RT} \cosh\left(\frac{2F\varphi}{2RT}\right)} \quad (2.5)$$

where A is surface area, ε is the dielectric constant, Z is the ionic charge number, φ is overvoltage, the voltage across the double-layer, c is the density of the ions, R is the gas constant, F is the Faraday constant, and T is the absolute temperature. Later in 1924, Stern improved the Gouy-Chapman model by adding a compact layer. Stern combined the both Helmholtz capacitance and diffused layer (Gouy-Chapman) capacitance in series connection [28], which led to the following double-layer capacitance expression:

$$C_s = \frac{1}{\left(\frac{1}{C_H} + \frac{1}{C_{GC}}\right)} \quad (2.6)$$

2.4 Structure of Supercapacitors

The functional components composing the basic structure of a supercapacitor are electrode materials, electrolyte solution, and separator. The basic structure of charged and uncharged supercapacitor is described in Figure 2.6. These components have a significant impact on the supercapacitor operation and performance. A brief review of these components will be given in the following subsections. The interested reader can find comprehensive discussion of these components and their classifications in [29].

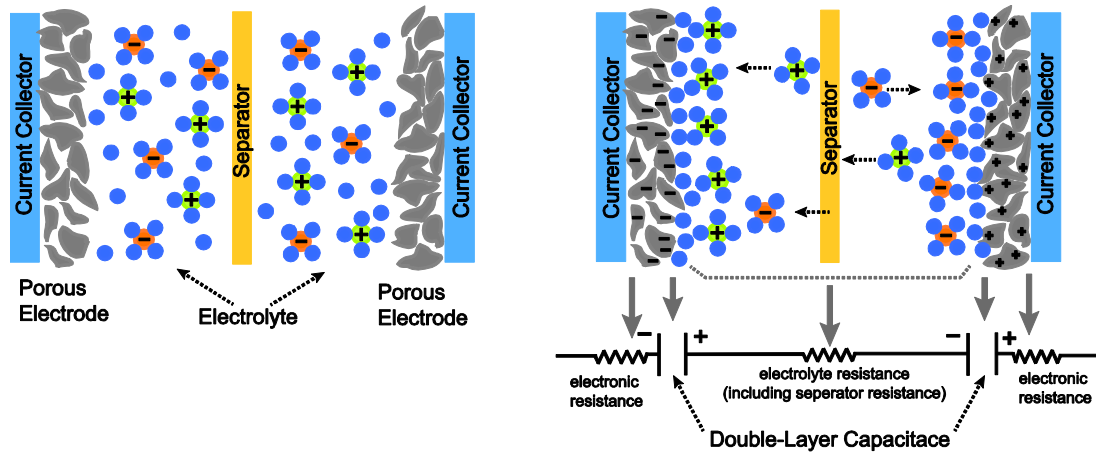


Figure 2.6 The basic structure of the supercapacitor modified from [19]

2.4.1 Electrode materials

The surface characteristics of the electrode materials considerably affect the double-layer capacitance. The most widely used electrode materials in a supercapacitor are carbons, and metal oxides. As shown in Figure 2.6, electrodes are connected to current collectors, which are also enclosed with external metal leads to compose the negative and positive terminals of the device.

Carbon is the most popular electrode material for supercapacitors due to its low price, high surface area, commercial availability, and high electrochemical stability. It is possible to have high-surface area of up to $2500 \text{ m}^2/\text{g}$ with carbons in different forms such as glass, powder, fiber, foam, nanotubes and carbon aerogels [18], [29], [30]. One may assume that the specific capacitance can be increased proportionally as the surface area of carbon-based electrode is increased. However, this is not true because the surface area is not the only factor influencing the capacitance. The accessibility of the electrolyte ions to the porous electrode also has significant influence on the capacitance. If the pore size is kept very small to achieve high-surface area electrodes, the mobility of electrolyte ions through the pores will decrease. Hence, manufacturing porous electrodes possessing very small pores will not increase the capacitance. Therefore, the pore size must be chosen according to the type of electrolyte solution in such a way that the ions can easily access to the deeper sides of the pores while keeping the surface

area in high levels. There is another tradeoff between energy and power density because of the size of the pores. The conductivity of the electrode material has a direct influence on power density, but it is inversely proportional to particle size. Although the small particles are desirable for higher capacitance they increase the internal resistance, which limits the power density. Power density can be increased with activated carbon electrodes possessing larger pores. On the other hand, this will decrease achievable charge storage due to reduced surface area [18].

Metal oxides, e.g., RuO_2 and IrO_2 , are also utilized as an electrode material in the supercapacitors. They were mostly used in electrode materials in early supercapacitors utilized for space and military applications [30] because of their high specific capacitance and low resistance, which resulted in very high powerful supercapacitors. For example, the US Army Research Lab has built supercapacitor cells with an energy density of 8.5 Wh/kg and a power density of 6 kW/kg [32]. These supercapacitors, however, are too costly and their nominal cell voltages are relatively low, typically around 1V [15].

2.4.2 Electrolytes

The type of electrolyte also has a significant impact on the characteristics of the supercapacitors. The achievable voltage of a cell depends upon the breakdown voltage of the electrolyte. As expressed in Equation (2.2), the cell voltage has a direct relationship with the possible energy density. Moreover, power density is dependent on electrolyte conductivity because most of equivalent series resistance comes from the electrolyte. The most common types of electrolytes are: organic and aqueous electrolytes.

Organic electrolytes are the most attractive electrolytes due to their higher dissociation voltage. These electrolytes allow manufacturers to produce supercapacitors operable at voltages in the range of 2-2.7 [15]. However, organic electrolytes have a considerably high specific resistance, which limits the cell power. Compared to organic electrolytes, aqueous electrolytes have a lower breakdown voltage, usually 1 V, but they offer better conductivity [15]. Thus, the supercapacitors using aqueous electrolytes can achieve relatively higher power densities. As previously discussed, since the charge capacity of a supercapacitor depends upon the

accessibility of the ions to the pores on the surface of the electrode, the size of the ion and pore must be optimized to achieve the best pore size distribution. To summarize, the capacitance, energy density, and power density of a supercapacitor is greatly influenced by the type of electrolyte.

2.4.3 Separator

The separator is used to prevent the electrical contact between the two electrodes, but thanks to its porous structure, it allows ionic charge transfer. The types of the separators currently used in supercapacitors are polymer or paper separators, which can be utilized with organic electrolytes, and ceramic or fiber separators, which are usually used with aqueous electrolytes. For high supercapacitor performance, the separator must have high electrical resistance, high ionic conductance, and a small thickness [33].

CHAPTER 3

SUPERCAPACITOR CHARACTERIZATION AND MODELING

3.1 Characterization of Supercapacitor

The power analysis of HEVs under normal operation explores that frequent charge-discharge pulses are mostly required within the short time durations of acceleration and braking [34]. As already mentioned, these discontinuous power requirements are met by supercapacitors within time ranges varying from a few milliseconds to tens of seconds. It is, therefore, significant to understand the dynamic behavior of supercapacitors in case of HEV applications. For this reason, researchers in the field of supercapacitors have followed different methodologies for the characterization of the supercapacitors in order to better understand the supercapacitor electrical behavior. These methodologies can be classified as constant power test, constant current test, voltamperometry test, and impedance spectroscopy test [34], [35]. Among these methods, impedance spectroscopy test is the most convenient, effective, easy and accurate method [34]. In this research, electrochemical impedance spectroscopy (EIS) test is performed on a 2 kF Maxwell supercapacitor and the results are given in this section. Experimental procedure for EIS is explained in subsection 3.1.1. Analysis of the measurements is discussed in subsection 3.1.2. Finally, voltage dependency is studied in subsection 3.1.3.

3.1.1 Electrochemical Impedance Spectroscopy

EIS is used for characterization of the electrochemical behavior of energy storage devices. It is an excellent tool for studying the frequency response of the electrode materials. The EIS measurements have been, therefore, performed by several researchers to characterize the electrode materials in batteries, supercapacitors and fuel cells [13], [17], [36]. During the EIS analysis, a frequency sweep is performed on the supercapacitor within a certain frequency

range. The test is carried out at various voltage levels in order to investigate the dependency of the dynamic behavior of the supercapacitor to operating voltages.

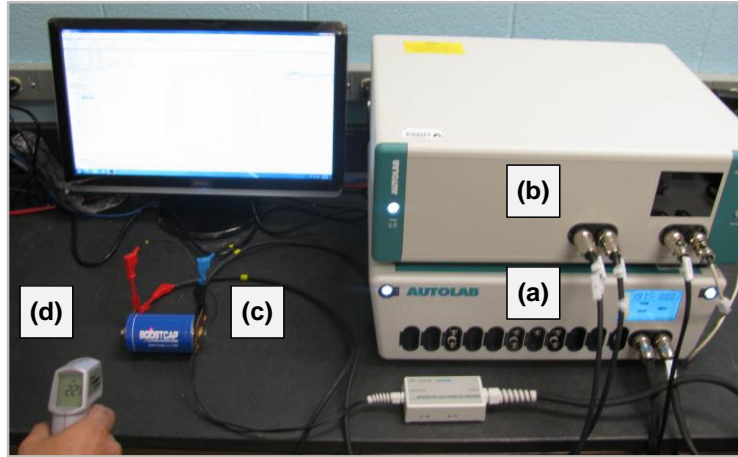


Figure 3.1 Test bench overview: (a) Metrohm Autolab PGSAT 302N (b) Current booster (c) Maxwell BCAP2000 supercapacitor (d) Laser thermometer

The experimental test bench, shown in Figure 3.1, is set up and the data is recorded for a Maxwell Technologies BCAP2000, with nominal capacitance of 2 kF and rated voltage of 2.7 V. In this experiment, the impedance data are recorded at different dc voltages varying from 0 to 2.5 V and at the room temperature of 22 °C. A Metrohm Autolab PGSAT 302N with a FRA module and current booster is used to measure the impedance and charge the supercapacitor. In addition, a laser thermometer is used to measure the temperature. After biasing the supercapacitor at the desired level, a small amplitude ac voltage (typically 5 mV)

$$U_{AC}(t) = U_0 \sin(\omega t) \quad (3.1)$$

is supplied to the supercapacitor. The resulting current amplitude and its phase are measured with respect to the applied voltage over a wide frequency range, from 10 mHz to 10 KHz.

$$I_{AC}(t) = I_0 \sin(\omega t - \phi) \quad (3.2)$$

These EIS measurements are then used to calculate the real and imaginary part of the impedance as shown by the following fundamental impedance equation:

$$Z(\omega) = \frac{U(\omega)}{I(\omega)} = |Z(\omega)|e^{j\phi} \quad (3.3)$$

3.1.2 Analysis of Impedance Spectroscopy Measurements

Through the subsections of this chapter the impedance data recorded at the fixed dc bias voltage of 2.5 V and at a room temperature of 22 °C will be used to explore the characteristics of the supercapacitors. The experimentally recorded real and imaginary parts of the impedance are plotted as a function of frequency on a log-log scale in Figure 3.2. The results clearly show that the real and imaginary part of impedance changes as a function of frequency.

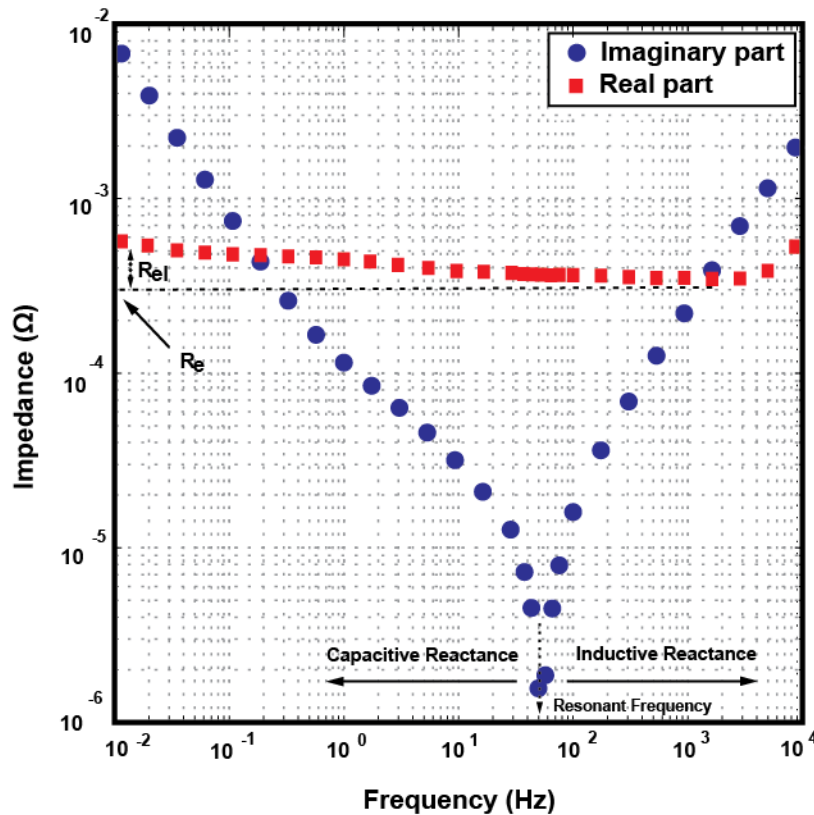


Figure 3.2 Imaginary and real part of supercapacitor impedance as a function of frequency with bias voltage of 2.5 V and a temperature of 22 °C

The squares in Figure 3.2 show the experimental data for the real part of impedance. As can be seen, the series resistance reduces as the frequency decreases. For frequencies lower than 10 mHz, the real part increases substantially due to the self-discharge, which is the result of the leakage current and internal charge distribution [35]. Supercapacitors used in HEVs are operable during short time ranges; however the supercapacitors self-discharge is characteristically observed in the order of hours. Thus, the self-discharge characteristic is usually

not driven with detailed parameters in many dynamic circuit models particularly developed for vehicular applications.

The frequency range between 10 mHz and 1 KHz gives the information on the equivalent series resistance (ESR). As the frequency reaches up to 1 KHz, the ESR slightly reduces down to its minimum value about 0.368 mΩ. This value represents the electronic resistance, R_e , between the electrode and the current collector metal. The real part variation of impedance within the frequency ranges from 10 Hz down to 10 mHz is described by the electrolyte resistance, R_{el} , inside the electrolyte solution. This variation can be justified by the fact that as the frequency decreases, ions can easily reach the deeper zones of the activated carbon pores, and consequently, their longer displacement within the electrolyte results in higher electrolyte resistance [29]. The characteristics of electrolyte resistance will be discussed in greater detail in subsection 3.2.1. Lastly, the supercapacitor inductance and parasitic inductance of all the connecting cables are responsible for the increase at frequencies higher than 1 KHz [36]. In HEV applications, the frequency range of the current profiles applied to supercapacitor is mostly between 10 mHz and 1 KHz, therefore the resistance variation at frequencies higher than 1 KHz is unnecessary to model.

The circles in Figure 3.2 represent the imaginary part of impedance obtained from EIS. The imaginary part can be evaluated based on the resonance frequency value, which has been found to be approximately 50 Hz. The investigated supercapacitor behavior becomes inductive at any frequency higher than 50 Hz and capacitive at any frequency lower than 50 Hz. The supercapacitor equivalent series inductance can be calculated in the high frequency range ($f > 50$ Hz) with the following equation:

$$L_s \approx \text{Im}(Z) / 2 \cdot \pi \cdot f \quad 3.4$$

Then, the double-layer capacitance value can be determined using the known inductance value in the following expression:

$$C_{dl} = 1 / 2 \cdot \pi \cdot f (2 \cdot \pi \cdot f \cdot L - \text{Im}(Z)) \quad 3.5$$

where L_s is the inductance, f is the frequency, and Z is the impedance [7].

3.1.3 Voltage and Thermal Dependence

In contrast to the electrolyte capacitor, where the capacitance variation is linear regardless of voltage variation, the supercapacitor capacitance changes with bias voltage. As depicted in Figure 3.3, the imaginary part of the impedance decreases when the voltage level increases from 0 to 2.5 V. This result also indicates that the capacitance value of the supercapacitor increases when the bias voltage level is increased and reaches its maximum value at low frequency of 10 mHz.

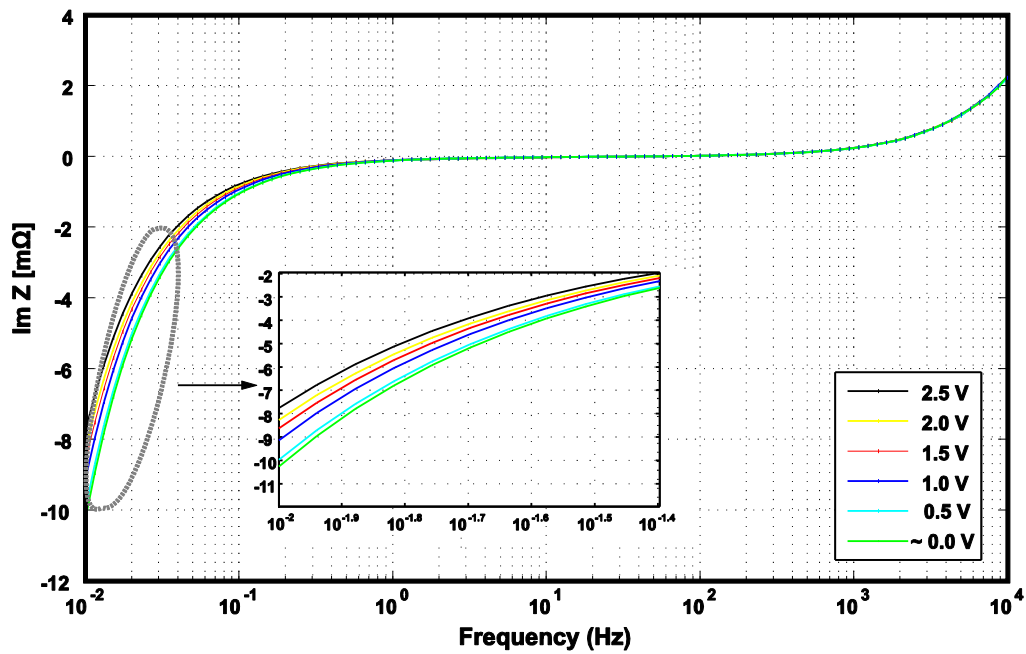


Figure 3.3 The imaginary part of supercapacitor impedance for different bias voltages vs. frequency

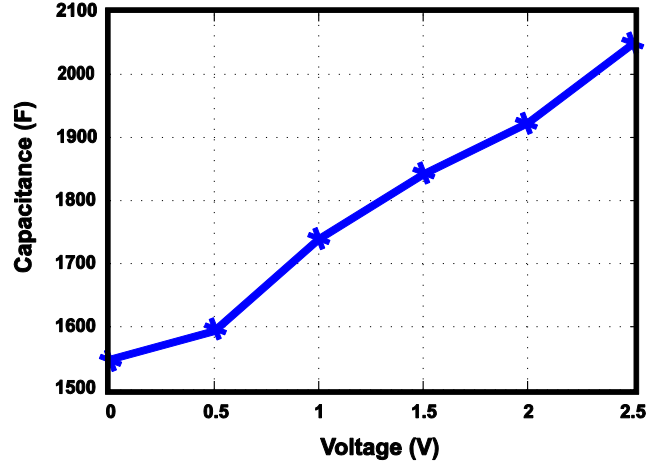


Figure 3.4 The supercapacitor capacitance as a function of voltage at 22 °C

Figure 3.4 represents this variation with voltage levels varying from 0 to 2.5 V. The increase in capacitance can be explained by either the decrease of the distance separating the charges or the increase of the dielectric constant of the electrolyte [36]. The total supercapacitor capacitance can be simply expressed by the following equation:

$$C_{sc} = C_0 + C(V) \quad (3.6)$$

where the C_0 is the capacitance at $V=0$, and $C(V)$ takes the capacitance variation into account. The precision in modeling can be improved by taking the capacitance variation into account. Moreover, the ESR slightly decreases with increasing voltage level as represented in Figure 3.5

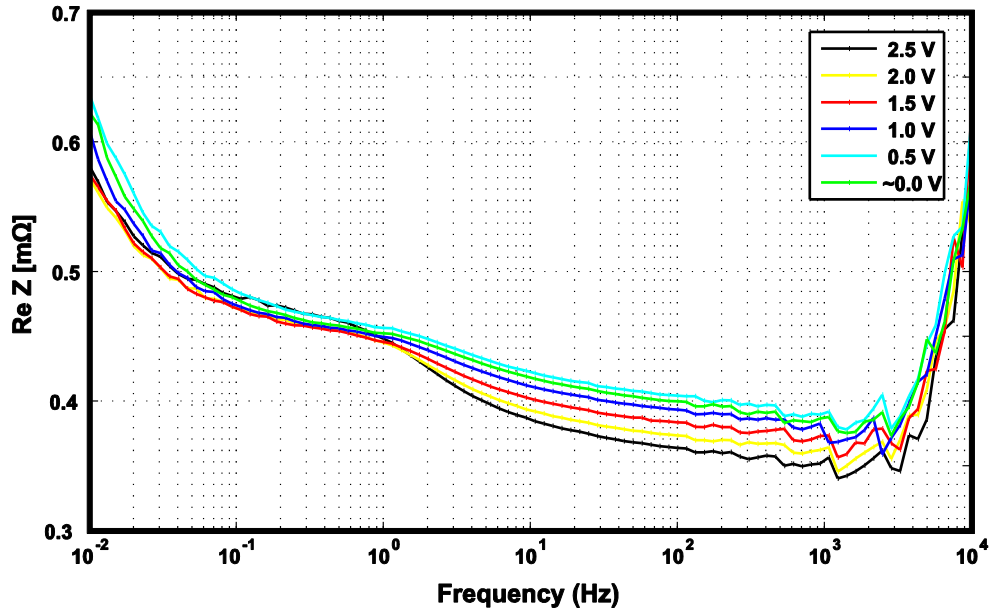


Figure 3.5 Measurement of the supercapacitor resistance at various bias voltages of 0.002, 0.5, 1, 1.5, 2.0 and 2.5 V and a temperature of 22 °C

The supercapacitors particularly used in vehicular applications are naturally exposed to different temperature levels. Therefore, it is also necessary to investigate the electrochemical behavior of supercapacitors under different operating temperatures to improve the preciseness of supercapacitor modeling. In the low frequency range of voltage disturbances, the ESR gently increases when the temperature decreases. Furthermore, the capacitance remains intact when the temperature changes [36].

In conclusion, the capacitance depends only on the operating voltage, while the ESR depends on both operating voltage and temperature. In this research, the dependency of capacitance and ESR on the operating voltage has been studied. Regarding the dependency of the parameters on temperature, this paper only relies on previous studies due to the lack of necessary technical equipment. Therefore, the parameters of circuit-based models that will be investigated in the following chapters will be determined with the impedance data recorded at constant temperature of 22 °C.

3.2 Modeling of Supercapacitor

To design a well-optimized ESU for HEVs during simulation-based analysis, one needs an equivalent circuit model describing dynamic behavior of the supercapacitors precisely. For this reason, many researchers have devoted their studies to the equivalent circuit models of supercapacitor [7], [13], [17], [35]-[37]. These circuit- models are aimed to be integrated into the practical simulators in order to allow designers easily find the best control strategy for the ESU.

3.2.1 Overview of existing equivalent circuit models

The supercapacitors are constructed in such a way that the electrode-electrolyte interface is distributed in space with porous electrode materials in order to maximize the surface area. The electrolyte resistance and double-layer capacitance spread deeply into the electrode pores. As a result, instead of a single capacitor, which is charged and discharged in linear fashion, a theoretical model composed of nonlinear capacitors and resistors, as shown in Figure 3.7, has been proposed [38]. Even though theoretical model helps to understand the physical phenomena, it is very complex for practical usage and includes many undetermined parameters. As shown in Figure 3.8, a classical RC model has been, thus, proposed for simplicity. It comprises three main parameters: a capacitor, C_{dl} , an equivalent series resistance (ESR), and an equivalent parallel resistance (EPR). ESR and EPR model ohmic loss during charge-discharge and the impact of the leakage current in the long term performance, respectively.. Due to its simple topology, it can be easily integrated into many systems and can be quickly simulated. Besides that, the parameter identification is relatively easier among the other equivalent circuit models. However, the classical RC model shows high accuracy only in low frequency applications. It is inadequate to model the supercapacitor behavior at high frequencies [12]. Therefore, more detailed circuit models displaying satisfactory accuracy in a wide frequency range have been proposed: three-branch model [13], transmission line model [37] and parallel RC model [17].

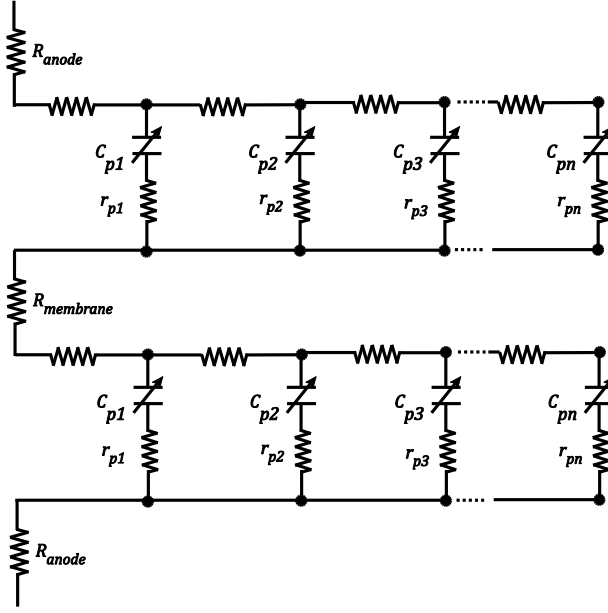


Figure 3.6 The supercapacitor theoretical model

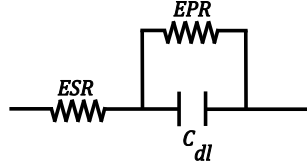


Figure 3.7 The supercapacitor classical RC model

In 2000 Zubieta and Bonert developed a nonlinear three-branch circuit model for power electronic applications [13]. They incorporated a nonlinear capacitance, C_f , varying as a function of terminal voltage to consider the bias voltage dependency of capacitance, as shown in Figure 3.9. The charge redistribution in pore sections through the electrode-electrolyte interface is also considered by adding additional RC branches. These branches are determined in such a way that each has well different time constant. The first branch, which has much lowest time constant, models the fast charge- discharge behavior in the time range of few seconds. The second branch is referred as delayed branch and usually models the behavior over the range of few minutes. Lastly, the third branch, also known as slow branch, models self-discharge behavior for time longer than 10 minutes. In addition to the RC branches, a leakage resistor has been included parallel to RC branches to govern leakage current effect. The model displays

acceptable accuracy in time range of 30 minutes at voltage levels above 40% of the rated terminal voltage [13]. For longer time and lower terminal voltage, its simulation results do not match with measured data. In this research, for more precise analysis, we will utilize the equivalent circuit models developed based on the porous structure of the Supercapacitor: transmission line and parallel RC branch model.

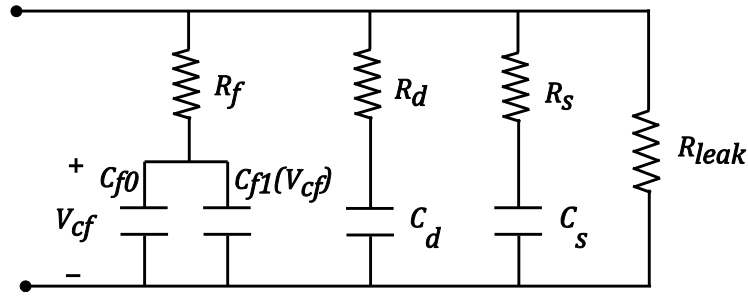


Figure 3.8 Three-branch equivalent circuit model of supercapacitor developed by Zubeta and Bonert

3.2.2 Porous Electrode Theory

The porous structure of an electrode has significant effects on characteristics of the supercapacitor. An extensive analysis of the porous electrode has been first conducted by de Levie to explore the effect of porosity on the electrolyte resistance and double layer capacitance [37]. In 1963, the same researcher developed the Porous Electrode Theory. According to this theory, the impedance of a single pore in the electrodes is adequate to investigate the porous behavior if all pores on the electrodes are assumed to be identical, cylindrical, and not interconnected. Additionally, the total impedance on both porous electrodes is assumed to be the same. Figure 3.9 (a) and (b) illustrates the internal structure of supercapacitor and a small section of a porous electrode including ideal cylindrical pores, respectively. Considering the aforementioned assumptions, the impedance behavior of a single cylindrical pore of length l can be represented by homogeneously distributed electrolyte resistance r_{el} and double layer capacitance c_{dl} . A single cylindrical pore of length l with distributed RC network is shown in Figure 3.9 (c).

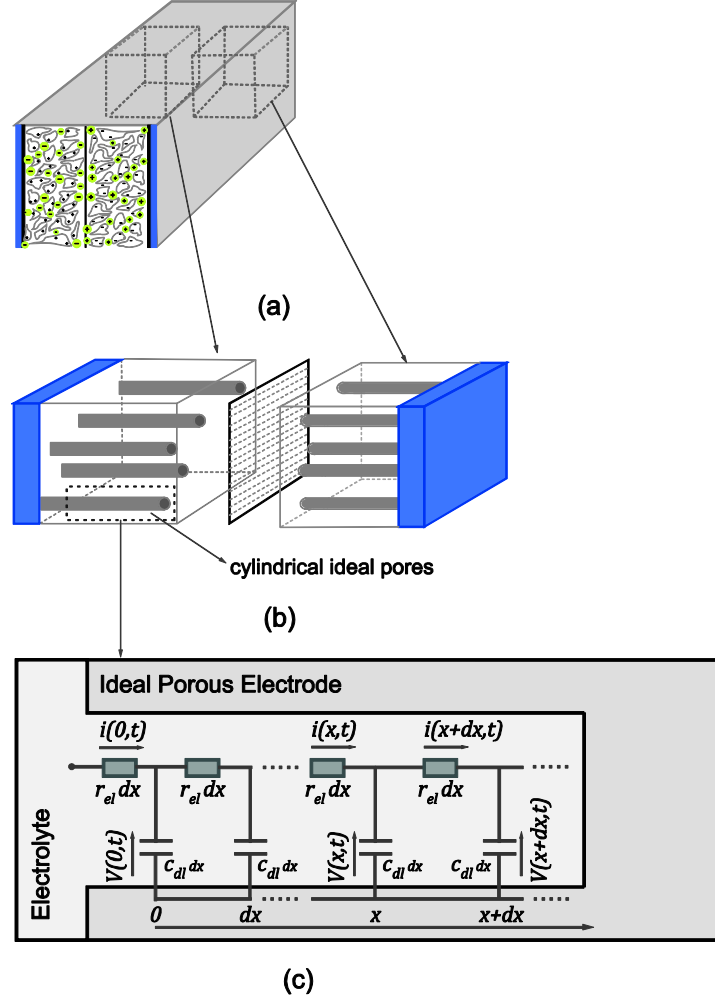


Figure 3.9 (a) A small structure of supercapacitor (b) 3-D visualization of ideal porous electrode (modified from [19]) (c) Distributed model of a single pore

Assuming that r_{el} and c_{dl} are the electrolyte resistance and the double-layer capacitance per unit length dx of the pore, respectively, the analytical expression of the pore impedance is calculated by linking the current $i(t, x)$ and the voltage $V(t, x)$ equations as following:

$$\frac{\partial V(t, x)}{\partial x} = -r_{el} \cdot i(t, x) \quad (3.7)$$

$$\frac{\partial i(t, x)}{\partial x} = -c_{dl} \cdot \frac{\partial V(t, x)}{\partial t} \quad (3.8)$$

The resulting impedance is:

$$Z_p = \sqrt{\frac{r_{el}}{j \cdot \omega \cdot c_{dl}}} \cdot \coth\left(\sqrt{j \cdot \omega \cdot c_{dl} \cdot r_{el} \cdot l}\right) \quad (3.9)$$

The local electrolyte resistance r_{el} and double-layer capacitance c_{dl} can be replaced with

$$R_{el} = r_{el} \cdot l \quad (3.10)$$

$$C_{dl} = c_{dl} \cdot l \quad (3.11)$$

The resulting impedance of the pore is [37]:

$$Z_p = \sqrt{\frac{R_{el}}{j \cdot \omega \cdot C_{dl}}} \cdot \coth\left(\sqrt{j \cdot \omega \cdot C_{dl} \cdot R_{el}}\right) \quad (3.12)$$

Considering the limiting cases for $\omega \rightarrow 0$ and $\omega \rightarrow \infty$

$$\coth x = \frac{1}{x} + \frac{1}{3}x + O(x^3) \text{ for } x \rightarrow 0 \text{ (Taylor expansion)} \quad (3.13)$$

$$\lim_{x \rightarrow \infty} (\coth x) = 1 \quad (3.14)$$

the Equation (3.9) can be simplified into the complex pore impedance at low and high frequencies as following in Equation (3.15) and Equation (3.16) :

$$Z_p(\omega \rightarrow 0) = \sqrt{\frac{R_{el}}{j \cdot \omega \cdot C_{dl}}} \cdot \left[\frac{1}{\sqrt{j \cdot \omega \cdot C_{dl} \cdot R_{el}}} + \frac{\sqrt{j \cdot \omega \cdot C_{dl} \cdot R_{el}}}{3} \right] = \frac{1}{j \cdot \omega \cdot C_{dl}} + \frac{R_{el}}{3} \quad (3.15)$$

$$Z_p(\omega \rightarrow \infty) = \sqrt{\frac{R_{el}}{j \cdot \omega \cdot C_{dl}}} \quad (3.16)$$

As also can be understood from the simplified Equation (3.15), in the low frequency band the impedance curve becomes perpendicular to the real axis, which implies the pure capacitive behavior. As the frequency increases, the impedance curve makes an angle of 45° with the real axis (see Equation 3.16) and crosses the real axis at the resonance frequency. Two independent parameters (L_s and R_e) are also added to the porous impedance Z_p to model the inductive behavior and electronic resistance (also known as high frequency resistance) of the supercapacitor, respectively. Consequently, the equivalent circuit can be driven by the following

parameters: an inductance L_s , an electronic resistance R_e , pore impedance Z_p . Figure 3.11 depicts the equivalent circuit model of the supercapacitor.

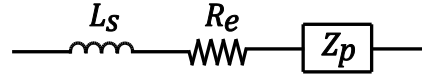


Figure 3.10 The equivalent circuit model based on the Porous Electrode Theory

Based on the Porous Electrode Theory, two proposed equivalent circuit models, transmission line model and RC parallel-branch model, have been proposed.

3.2.2.1 Transmission Line Model of Pore Impedance

The simplest way to implement the pore impedance Z_p into the simulators is to use the transmission line topology from which Equation (3.12) has been calculated. Figure 3.11 shows the corresponding equivalent circuit model, namely transmission line model (TLM). TLM has been used for supercapacitor modeling in several applications due to following advantages:

- It physically captures the distributed nature of the supercapacitor and takes into account both dynamic and longtime behaviors.
- Experimental data can be easily fitted to its performance within a wide range of frequencies.
- It can be easily adapted to other system simulation software tools to find numerical and analytical solutions [4].

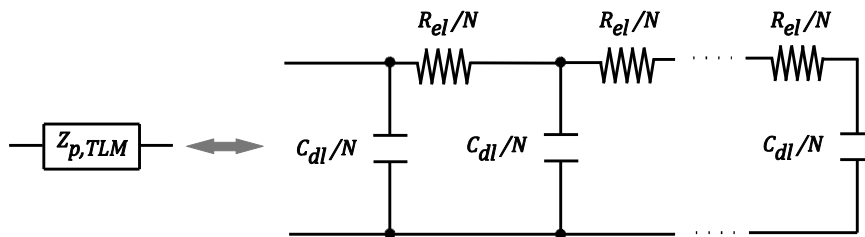


Figure 3.11 The transmission line model of pore impedance

3.2.2.2 RC parallel-branch Model of Pore Impedance

The RC parallel-branch model has been proposed by Buller based on the Porous Electrode Theory. Figure 3.12 illustrates the RC parallel-branch model. Buller simply used an alternative analytical representation of the pore impedance by employing the pulse response of Z_p .

$$Z_p = \sqrt{\frac{R_{el}}{j \cdot \omega \cdot C_{dl}}} \cdot \coth(\sqrt{j \cdot \omega \cdot R_{el} \cdot C_{dl}}) \Leftrightarrow \frac{1}{C_{dl}} + \frac{2}{C_{dl}} \sum_{n=1}^{\infty} e^{\frac{-n^2 \cdot \pi^2}{R_{el} \cdot C_{dl}} t} \quad (3.17)$$

With the pulse response of a parallel RC branch

$$\sqrt{\frac{R}{j \cdot \omega \cdot C}} \Leftrightarrow \frac{1}{C} \cdot e^{\frac{-t}{RC}} \quad (3.18)$$

The resulting parameters of the pore impedance can be written as

$$R_k = \frac{2R_{el}}{\pi^2 \cdot k^2}, k = 1..n \quad (3.19)$$

$$C_1 = C_2 = \dots = C_n = C_{dl}/2 \quad (3.20)$$

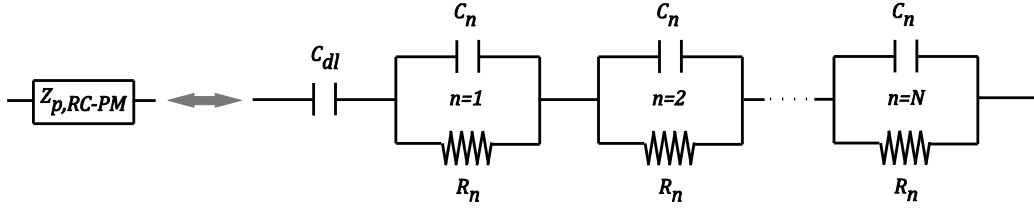


Figure 3.12 The RC paralel-branch model of pore impedance

In addition to the advantages presented by TLM, the RC parallel-branch model displays faster convergence in simulations as well. The main difference between these two models is the different analytical representation of the pore impedance. In both circuit models, as the number of RC branches increases, they characterize the porous nature of the supercapacitor more precisely. Accordingly, simulation results show a better agreement with the measured data. However, that results in higher order models displaying high computational cost in simulations.

In the following chapters, the order reduction techniques and waveform relaxation methods will be applied to high-order RC parallel-branch model and five-stage TLM, respectively.

CHAPTER 4

REDUCED ORDER ANALYSIS OF HIGH-FIDELITY RC PARALLEL-BRANCH MODEL OF SUPERCAPACITOR

4.1 Order Reduction Theory

The order reduction process is used to simplify the complexity of high-order systems by replacing the original high-order state space with a lower-order space. In this way, systems can be easily controlled, efficiently optimized, and rapidly simulated. Several researchers have devoted their studies to the order reduction and model specification: Newton [39], Taylor [40], Euler [41], Lagrange [42], and Fourier published their work on model simplification and function approximation in 1704, 1715, 1755, 1759, and 1807, respectively. Pade's PhD dissertation and his approximations were published in 1892 [43]. Lanczos [44], Arnoldi [45], Saad/Schultz [46], and Fletcher [47] developed their iterative methods, basics of moment-matching Krylov subspace techniques, in 1950, 1951, 1976, and 1986, respectively. Moore presented truncated balanced realization (TBR) [48] in 1981, and Glover published his well-known work on Hankel-norm reduction [49] in 1984. Proper orthogonal decomposition was first presented by Sirovich in 1987 [50]. Different classes of Krylov subspaces methods, explicit moment matching (asymptotic waveform evaluation introduced in 1990 [51]) and implicit moment matching (Pade via Lanczos introduced by Freund in 1993 [52] and Pade via Arnoldi introduced by Silveria in 1995 [53]) presently dominate the order-reduction realm. In the literature, order reduction techniques has been used to alleviate the computational intensity of high-fidelity magnetic equivalent circuit models and equivalent circuit models of supercapacitors [54]-[58].

In this research, the model-order reduction techniques are only used as tools to extract the low order dynamic model of the high-order RC parallel-branch equivalent circuit model of supercapacitors. For this reason, the theoretical features of reduction techniques are beyond the

scope of this thesis. Among the linear reduction tools in the literature, only the most widely used techniques, Balanced-order and Krylov-subspace methods, will be examined and used throughout the thesis. Prior to the discussion of the investigated reduction techniques, this chapter first focuses on the analysis of the high-order equivalent circuit model and the derivation of the state space model.

4.2 Analysis of High-Fidelity RC Parallel-branch Model

In order to emphasize on the capability of handling higher frequency dynamics, the equivalent circuit model proposed by Buller has been renamed to high-fidelity model for the rest of the chapter. Based on the physical structure of the supercapacitor, the derived high-fidelity circuit model is shown in Figure 4.1, which can be also expressed by the following equation:

$$Z_p = j \cdot \omega \cdot L_s + R_e + \sqrt{\frac{R_{el}}{j \cdot \omega \cdot C_{dl}}} \cdot \coth(\sqrt{R_{el} \cdot C_{dl}} \cdot j \cdot \omega) \quad (4.1)$$

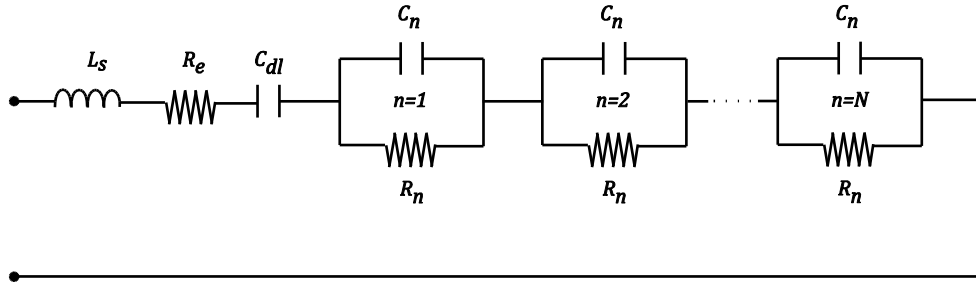


Figure 4.1 High-fidelity RC parallel-branch model of supercapacitor.

As already mentioned in previous chapter the parameters of the RC branches are identified by the following expressions.

$$R_1 = R_2 = \dots = R_n, R_n = \frac{2R_{el}}{\pi^2 \cdot n^2} \quad (4.2)$$

$$C_1 = C_2 = \dots = C_n = C_{dl} / 2 \quad (4.3)$$

In order to achieve an equivalent circuit model with validated parameters (L_s , R_e , C_{dl} and R_{el}) the impedance spectrum data will be taken into account. Figure 4.2 shows the measured impedance data in Nyquist plane at the voltage level of 2.5 V.

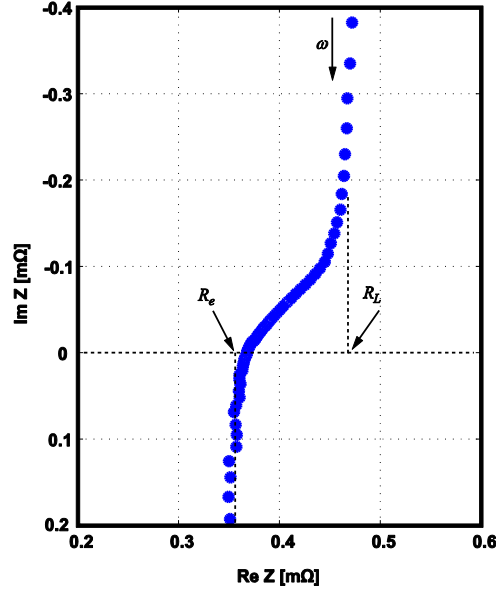


Figure 4.2 The Nyquist plot of the measured impedance of 2 kF supercapacitor at 2.5 V, 22 °C

The unknown parameters can be determined based on the impedance spectrum data as shown in Figure 4.2. For the sake of the simple parameter identification, Equation (4.1) can be simplified by considering the limiting cases of the impedance curve. Also, as shown in Figure 4.2, the impedance curve demonstrates perpendicular behavior to the real axis at low and high frequencies. Recalling Equation (3.15) for the low frequency band, Equation (4.1) reduces to

$$Z_{SC}(\omega \rightarrow 0) = j \cdot \omega \cdot L_s + \frac{1}{j \cdot \omega \cdot C_{dl}} + R_L \quad (4.4)$$

where R_L , the total equivalent resistance of the supercapacitor at low frequencies, is defined

$$R_L = R_e + \frac{R_{el}}{3} \quad (4.5)$$

In high frequency band, using Equation (3.16), Equation (4.1) can be reduced to

$$Z_{SC}(\omega \rightarrow \infty) = j \cdot \omega \cdot L_s + R_e + \sqrt{\frac{R_{el}}{j \cdot \omega \cdot C_{dl}}} \quad (4.6)$$

As can be seen from Equation (4.6), the term including electrolyte resistance R_{el} is negligible at high frequencies and consequently the equation can be further simplified to the following expression:

$$Z_{SC}(\omega \rightarrow \infty) = j \cdot \omega \cdot L_s + R_e \quad (4.7)$$

Thus, the electronic resistance, R_e , and the series inductance, L_s , can be easily determined at high frequencies. The R_{el} can be determined with the known R_e at low frequencies by using Equation (4.5). The double-layer capacitance C_{dl} can be calculated at low frequency of 10 mHz by recalling Equation (3.6) that has been derived in the previous chapter. In Figure 4.3 the measured impedance data is compared with the impedance predicted by high-fidelity model (60th order). In the determined frequency range, the two plots perfectly match with each other.

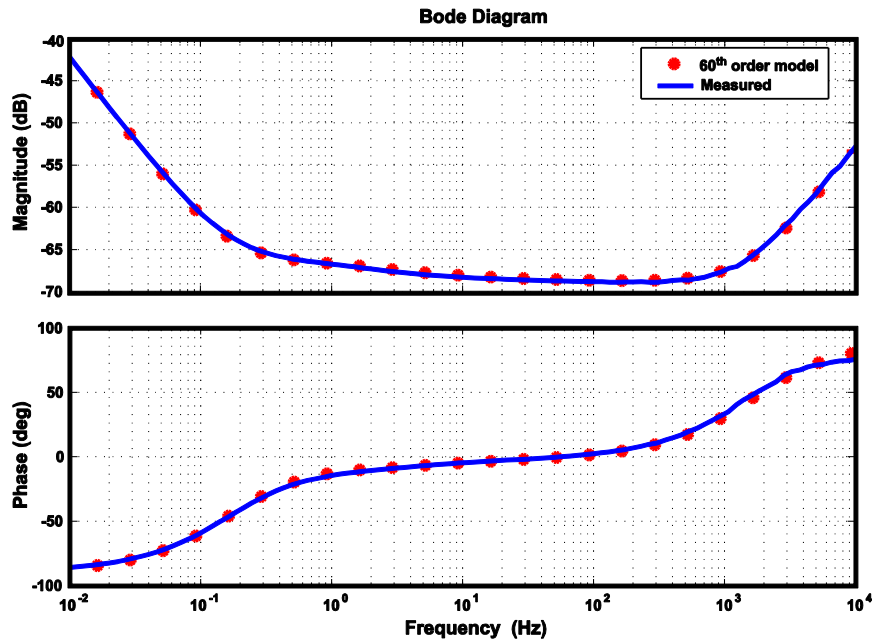


Figure 4.3 The bode plot of measured impedance and high-fidelity model impedance at 2.5 V, 22 °C.

The number of the RC branches determines the accuracy level of the equivalent circuit model. As shown in Figure 4.3, the high-fidelity circuit model shows better simulation results, which are in nearly perfect agreement with the measured data. However, the system becomes more complex, which leads to high computational cost in simulations. One solution to this problem is to reduce the system order by implementing order reductions techniques. The advantage of the reduction techniques is that a reduced circuit model displaying acceptable accuracy can be derived from the high-fidelity model. Figure 4.4 shows the overall process. First,

from the existing physical high-fidelity model, a high order state space model is derived. Next, the state-space model is reduced to a few dominant ODE's. It will be shown that the reduced order model is in an acceptable match with the original model.

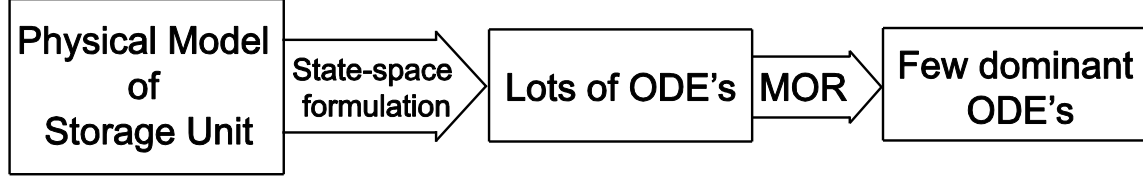


Figure 4.4 Block diagram of model order reduction process.

The state-space model of the high-fidelity circuit model, shown in Figure 4.1 is defined as

$$\begin{cases} \frac{d\mathbf{x}}{dt} = \mathbf{A}\mathbf{x} + \mathbf{B}\mathbf{u} \\ \mathbf{y} = \mathbf{C}\mathbf{x} + \mathbf{D}\mathbf{u} \end{cases} \quad (4.8)$$

where

$$\mathbf{x} = [x_1 \ x_2 \ \dots \ x_{n+2}]^T = [i \ V_{C_{dl}} \ V_{C_1} \ \dots \ V_{C_n}]^T \quad (4.9)$$

$$\mathbf{u} = [V_{in}], \mathbf{y} = [i] \quad (4.10)$$

n is the number of RC branches. The matrices $\mathbf{A}, \mathbf{B}, \mathbf{C},$ and \mathbf{D} in Equation (4.8) are

$$\mathbf{A} = \begin{bmatrix} -R_i/L & -1/L & -1/L & -1/L & -1/L & -1/L & \dots & -1/L \\ 1/C & 0 & 0 & 0 & 0 & 0 & \dots & 0 \\ 2/C & 0 & -2/(R_1C) & 0 & 0 & 0 & \dots & 0 \\ 2/C & 0 & 0 & -2/(R_2C) & \dots & 0 & \dots & 0 \\ 2/C & 0 & 0 & 0 & -2/(R_3C) & \vdots & \dots & 0 \\ 2/C & 0 & 0 & 0 & 0 & \ddots & \dots & 0 \\ \vdots & \vdots & \vdots & \vdots & \vdots & \vdots & \ddots & 0 \\ 2/C & 0 & 0 & 0 & 0 & 0 & \dots & -2/(R_nC) \end{bmatrix} \quad (4.11)$$

$$\mathbf{B} = [1/L \ 0 \ \dots \ 0]^T \quad (4.12)$$

$$\mathbf{C} = [1 \ 0 \ \dots \ 0] \quad (4.13)$$

$$\mathbf{D} = [0] \quad (4.14)$$

The transfer function of the system is defined as the input admittance of supercapacitor

$$\mathbf{H}(s) = \mathbf{D} + \mathbf{C}(s\mathbf{I} - \mathbf{A})^{-1}\mathbf{B} = \frac{\mathbf{y}(s)}{\mathbf{u}(s)} = \frac{i(s)}{V_{in}(s)} \quad (4.15)$$

Once the full order model is formulated, different order-reduction techniques can be considered to extract the low order model of supercapacitor.

4.3 Order Reduction Framework

The model order reduction will be utilized to reduce the order of the high-fidelity circuit model of supercapacitor. The standard state-space model of an equivalent circuit model can be presented by

$$\begin{cases} \frac{d\mathbf{x}}{dt} = \mathbf{A}\mathbf{x} + \mathbf{B}\mathbf{u}, & \mathbf{A} \in \mathbb{R}^{n \times n}, \mathbf{B} \in \mathbb{R}^{n \times p}, \mathbf{x} \in \mathbb{R}^n \\ \mathbf{y} = \mathbf{C}\mathbf{x} + \mathbf{D}\mathbf{u}, & \mathbf{C} \in \mathbb{R}^{p \times n}, \mathbf{D} \in \mathbb{R}^{p \times p}, \mathbf{u} \in \mathbb{R}^p \end{cases} \quad (4.16)$$

A model order reduction process seeks to replace Equation (4.16) with a similar system with Equation (4.17)

$$\begin{cases} \frac{d\mathbf{x}_r}{dt} = \mathbf{A}_r\mathbf{x}_r + \mathbf{B}_r\mathbf{u}, & \mathbf{A}_r \in \mathbb{R}^{n \times n}, \mathbf{B}_r \in \mathbb{R}^{n \times p}, \mathbf{x}_r \in \mathbb{R}^n \\ \tilde{\mathbf{y}} = \mathbf{C}_r\mathbf{x}_r + \mathbf{D}_r\mathbf{u}, & \mathbf{C}_r \in \mathbb{R}^{p \times n}, \mathbf{D}_r \in \mathbb{R}^{p \times p}, \mathbf{u} \in \mathbb{R}^p \end{cases} \quad (4.17)$$

The order of the reduced systems is, q much smaller than the original order, n . Meanwhile, for the input, $\mathbf{u}(t)$, the reduced-order model output, $\tilde{\mathbf{y}}(t)$, closely resembles the original output, $\mathbf{y}(t)$

$$\|\mathbf{y}(t) - \tilde{\mathbf{y}}(t)\| < \varepsilon \quad (4.18)$$

Likewise, transfer functions of systems in Equations (4.16) and (4.17) match for a given tolerance and frequency range

$$\begin{cases} \mathbf{H}(s) = \mathbf{D} + \mathbf{C}(s\mathbf{I} - \mathbf{A})^{-1}\mathbf{B} \\ \mathbf{H}_r(s) = \mathbf{D}_r + \mathbf{C}_r(s\mathbf{I} - \mathbf{A}_r)^{-1}\mathbf{B}_r \end{cases} \Rightarrow \|\mathbf{H}(s) - \mathbf{H}_r(s)\| < \varepsilon \quad (4.19)$$

The goal of order reduction is to find $\{\mathbf{A}_r \quad \mathbf{B}_r \quad \mathbf{C}_r \quad \mathbf{D}_r\}$ in Equation (4.17) or $\mathbf{H}_r(s)$ in Equation (4.19).

4.4 Balanced Order Reduction

In the balanced order reduction technique the system is transferred to a base where the states are hardly reachable and observable. Later, those states or associated dynamics are truncated. This is done by changing the system coordinates such that the observability and controllability Gramian matrices are equal. The state vector of the balanced system is ordered based on the contributions to the input-output relationship (Henkel singular values). Subsequently, the last (n, q) state variables, or their dynamics, are eliminated for a given cut-off Henkel singular value. The variables n and q are the model order for the full and reduced order models, respectively. In the truncated balanced residualization (TBR) method, unimportant state variables are set to zero. In singular perturbation approximation (SPA) method [59], one may set the derivative of the “unimportant states” to be zero. Both methods rely on the information obtained from the controllability, \mathbf{W}_c , and observability, \mathbf{W}_o , Gramians

$$\begin{cases} \mathbf{W}_c = \int_0^\infty e^{\mathbf{A}t} \mathbf{B} \mathbf{B}^T e^{\mathbf{A}^T t} dt \\ \mathbf{W}_o = \int_0^\infty e^{\mathbf{A}^T t} \mathbf{C}^T \mathbf{C} e^{\mathbf{A}t} dt \end{cases} \quad (4.20)$$

These Gramians are found by solving the following (dual) Lyapunov equations

$$\begin{cases} \mathbf{A} \mathbf{W}_c + \mathbf{W}_c \mathbf{A}^T = -\mathbf{B} \mathbf{B}^T \\ \mathbf{W}_o \mathbf{A} + \mathbf{A}^T \mathbf{W}_o = -\mathbf{C}^T \mathbf{C} \end{cases} \quad (4.21)$$

Hankel singular values are extracted as the square roots of the products of eigenvalues of two Gramians

$$\delta_i = \sqrt{\text{eig}(\mathbf{W}_c \mathbf{W}_o)}, i = 1..n \quad (4.22)$$

Hankel singular values contain useful information about the input-output relationship; the states with small singular values have a weaker effect on input-output relationships and most likely are less controllable/observable. Thus, states with smaller Hankel singular values can be removed. To accomplish this, one should use a change of coordinates to balance the system,

i.e., give it equal, diagonal Gramians. In particular, one may solve for a balancing transformation matrix \mathbf{T}

$$\begin{cases} \mathbf{W}_c \mathbf{W}_o \mathbf{T} = \mathbf{T} \Sigma^2 \\ \Sigma = \text{diag}\{\delta_1, \delta_2, \dots, \delta_n\} \end{cases} \quad (4.23)$$

This matrix then can be used to equate and diagonalize the Gramian matrices

$$\begin{cases} \mathbf{W}_c \rightarrow \mathbf{T}^{-1} \mathbf{W}_c \mathbf{T}^{-T} \\ \mathbf{W}_o \rightarrow \mathbf{T}^T \mathbf{W}_o \mathbf{T} \end{cases} \quad (4.24)$$

and to balance the state equations in Equation (4.16) by a change of coordinates

$$\begin{cases} \frac{d\tilde{\mathbf{x}}}{dt} = \tilde{\mathbf{A}}\tilde{\mathbf{x}} + \tilde{\mathbf{B}}\mathbf{u}, \quad \tilde{\mathbf{A}} = \mathbf{T}\mathbf{A}\mathbf{T}^{-1}, \tilde{\mathbf{B}} = \mathbf{T}\mathbf{B} \\ \mathbf{y} = \tilde{\mathbf{C}}\tilde{\mathbf{x}} + \tilde{\mathbf{D}}\mathbf{u}, \quad \tilde{\mathbf{C}} = \mathbf{C}\mathbf{T}^{-1}, \tilde{\mathbf{D}} = \mathbf{D} \end{cases} \quad (4.25)$$

In the resulting balanced system, the full state vector is balanced and partitioned based on state contributions to the input-output response (or corresponding Hankel singular values)

$$\tilde{\mathbf{x}} = \mathbf{T}\mathbf{x} = \begin{bmatrix} \tilde{\mathbf{x}}_1 \\ \vdots \\ \tilde{\mathbf{x}}_2 \end{bmatrix} \quad (4.26)$$

where $\tilde{\mathbf{x}}_1$ and $\tilde{\mathbf{x}}_2$ are the state variables associated with significant and small Hankel singular values, respectively. As discussed previously, supercapacitors are modeled with the input voltage, V_{in} , as the input variable, \mathbf{u} , and current, i , as the output variable, \mathbf{y} . Thus one may have a partitioned system as

$$\begin{cases} \frac{d\tilde{\mathbf{x}}}{dt} = \tilde{\mathbf{A}}\tilde{\mathbf{x}} + \tilde{\mathbf{B}}\mathbf{u} = \begin{bmatrix} \tilde{\mathbf{A}}_{11} & \tilde{\mathbf{A}}_{12} \\ \tilde{\mathbf{A}}_{21} & \tilde{\mathbf{A}}_{22} \end{bmatrix} \begin{bmatrix} \tilde{\mathbf{x}}_1 \\ \tilde{\mathbf{x}}_2 \end{bmatrix} + \begin{bmatrix} \tilde{\mathbf{b}}_1 \\ \tilde{\mathbf{b}}_2 \end{bmatrix} V_{in} \\ \mathbf{y} = \tilde{\mathbf{C}}\tilde{\mathbf{x}} + \tilde{\mathbf{D}}\mathbf{u} = \begin{bmatrix} \tilde{\mathbf{C}}_1 & \tilde{\mathbf{C}}_2 \end{bmatrix} \begin{bmatrix} \tilde{\mathbf{x}}_1 \\ \tilde{\mathbf{x}}_2 \end{bmatrix} + dV_{in} \end{cases} \quad (4.27)$$

From this point, one can use either the truncated balanced residualization (TBR) or singular perturbation approximation (SPA) approaches. In SPA, the reduced-order model is extracted by setting the derivative of the state variables with small Henkel singular values, $\tilde{\mathbf{x}}_2$, to zero and modifying Equation (4.27)

$$\begin{cases} \frac{d\tilde{\mathbf{x}}}{dt} = \underbrace{(\tilde{\mathbf{A}}_{11} - \tilde{\mathbf{A}}_{12}(\tilde{\mathbf{A}}_{22})^{-1}\tilde{\mathbf{A}}_{21})}_{\mathbf{A}_r} \tilde{\mathbf{x}}_1 + \underbrace{(\tilde{\mathbf{b}}_1 - \tilde{\mathbf{A}}_{12}(\tilde{\mathbf{A}}_{22})^{-1}\tilde{\mathbf{b}}_2)}_{\mathbf{B}_r} V_{in} \\ \mathbf{y} = \underbrace{(\tilde{\mathbf{C}}_1 - \tilde{\mathbf{C}}_2(\tilde{\mathbf{A}}_{22})^{-1}\tilde{\mathbf{A}}_{21})}_{\mathbf{C}_r} \tilde{\mathbf{x}}_1 + \underbrace{(d - \tilde{\mathbf{C}}_2(\tilde{\mathbf{A}}_{22})^{-1}\tilde{\mathbf{b}}_2)}_{\mathbf{D}_r} V_{in} \end{cases} \quad (4.28)$$

The resulting reduced order model does not match at very high frequencies, but the dc-gain match between the reduced and full-order models is guaranteed [60]

$$\mathbf{H}(0) = \mathbf{D} + \mathbf{C}(-\mathbf{A})^{-1}\mathbf{B} = \mathbf{D}_r + \mathbf{C}_r(-\mathbf{A}_r)^{-1}\mathbf{B}_r = \mathbf{H}_r(0) \quad (4.29)$$

In the TBR method, the reduced-order model is extracted by eliminating the state variables with small Henkel singular values, $\tilde{\mathbf{x}}_2$, and truncating Equation (4.27)

$$\begin{cases} \frac{d\tilde{\mathbf{x}}}{dt} = \tilde{\mathbf{A}}_1 \tilde{\mathbf{x}}_1 + \tilde{\mathbf{b}}_1 V_{in} \\ \mathbf{y} = \tilde{\mathbf{C}}_1 \tilde{\mathbf{x}}_1 + d V_{in} \end{cases} \quad (4.30)$$

The reduced and full order model transfer functions in Equation (4.19) do not match in DC, but converge to d at a very high frequency

$$\mathbf{H}(\infty) = d = \mathbf{H}_r(\infty) \quad (4.31)$$

Error bounds for the q^{th} order reduced model in the frequency domain can be calculated [61] as

$$\|\mathbf{H}(s) - \mathbf{H}_r(s)\| < 2 \sum_{k=q+1}^n \delta_k \quad (4.32)$$

TBR and SPA methods are projection-based and non-projection-based methods, respectively. Balanced order reduction method is appropriate for relatively small systems, e.g., less than 100 state variables. For large systems balancing and truncating the equations makes the reduction process computationally intractable.

4.5 Krylov-subspace method

Krylov-subspace methods are projection-based reduction techniques which basically project the higher order state space into a lower order space [62] - [64]. The state projection and order reduction can be written as

$$\begin{cases} \frac{d\mathbf{x}}{dt} = \mathbf{A}_r \mathbf{x}_r + \mathbf{B}_r \mathbf{u}, \quad \mathbf{A}_r = \mathbf{W}^T \mathbf{A} \mathbf{W}, \mathbf{B}_r = \mathbf{W}^T \mathbf{B} \\ \tilde{\mathbf{y}} = \mathbf{C}_r \mathbf{x}_r + \mathbf{D}_r \mathbf{u}, \quad \mathbf{C}_r = \mathbf{C} \mathbf{W}, \mathbf{D}_r = \mathbf{D} \end{cases} \quad (4.33)$$

where \mathbf{W} is the orthonormal projection matrix and is obtained from q th-order Krylov-subspace by utilizing the Arnoldi method [65], which is an orthogonal projection method.

$$\mathbf{K}_q(\mathbf{A}^{-1}, \mathbf{B}) = \text{span}\{\mathbf{B}, \mathbf{A}^{-1}\mathbf{B}, \dots, (\mathbf{A}^{-1})^{q-1}\mathbf{B}\} \quad (4.34)$$

where q refers to the order of the reduced system, which is lower than the order of the original system, n .

The construction of the one column of the projection matrix requires the iterative method. The iteration is initiated with the following normalized random vector

$$\mathbf{W}(:,1) = \frac{(\mathbf{A}^{-1}\mathbf{B})}{\|\mathbf{A}^{-1}\mathbf{B}\|} \quad (4.35)$$

The rest of the columns in projection matrix are extracted using the following steps. First, an initial vector is selected for the i^{th} column of projection matrix in the first loop where for $i = 2, \dots, q$

$$\mathbf{W}(:,i) = \mathbf{A}^{-1}\mathbf{W}(:,i-1) \quad (4.36)$$

Second, the orthonormal vector is generated by using the Gram-Schmidt procedure. For this, an inner loop is built where for $k = 1, \dots, i-1$

$$\mathbf{W}(:,i) = \mathbf{W}(:,i) - (\mathbf{W}(:,i))^T \mathbf{W}(:,k) \mathbf{W}(:,k) \quad (4.37)$$

$$\mathbf{W}(:,i) = \mathbf{W}(:,i) / \|\mathbf{W}(:,i)\| \quad (4.38)$$

Once the projection matrix is generated, the full-order state vector, \mathbf{x} , can be projected into a lower-order state vector by a similarity transform

$$\mathbf{x}_r = \mathbf{W}\mathbf{x}, \mathbf{x}_r \in \mathbb{R}^q, \mathbf{x} \in \mathbb{R}^n, \mathbf{W} \in \mathbb{R}^{q \times n} \quad (4.39)$$

where \mathbf{x}_r is the reduced-order state vector. The Krylov-subspace methods give accuracy results only in narrow frequency ranges, but they are mostly used in many system reduction processes due to their computational efficiency [66]. Both balanced order reduction (TBR and SPA) and

Krylov-subspace methods are adopted to extract the low order model of a supercapacitor in the following case studies.

4.6 Case Studies

A large parallel RC ladder structure is considered with the given circuit components and time constant values in Appendix A. The original model is of the 60th order, and is numerically reduced to 4 dominant state variables using the balanced reduction techniques (TBR and SPA) and Krylov-subspace technique. Figure 4.5 shows the excellent agreement between input impedances predicted by both the full-order and reduced order model extracted by SPA method. As can be seen in Figure 4.6, the 4th order reduced model extracted by TBR method also perfectly matches with the full-order model, but leads to a slight discrepancy at low frequencies ($f < 0.1$ Hz). In the case of the Krylov-subspace technique the 4th order reduced model displays an acceptable accuracy for low frequencies, as shown in Figure 4.7; however, it begins deviating at frequencies higher than the resonance frequency, 50 Hz.

It has been experimentally seen that the further reduced models (3th or 2nd order) extracted by all the reduction techniques investigated in this research do not have an acceptable match for practical usage. Figure 4.8 displays the comparison of the 4th order models reduced by all investigated reduction techniques. As already mentioned, since the supercapacitors used in vehicular power systems mostly function at the frequencies between 10 mHz and 1 KHz, the 4th order model extracted by the SPA method is the most suitable model. This reduced model can be used in simulation software tools in order to achieve acceptable results with less computational effort in simulations. As seen in Figure 4.9, the 4th order model reduced by the SPA is also compared with the 4th order model that is extracted from the original model without any order reduction by using only two RC branches. It is clear that the 4th order model reduced from the 60th order model shows higher accuracy than the original 4th order model, which proves the effectiveness of the adopted order-reduction method.

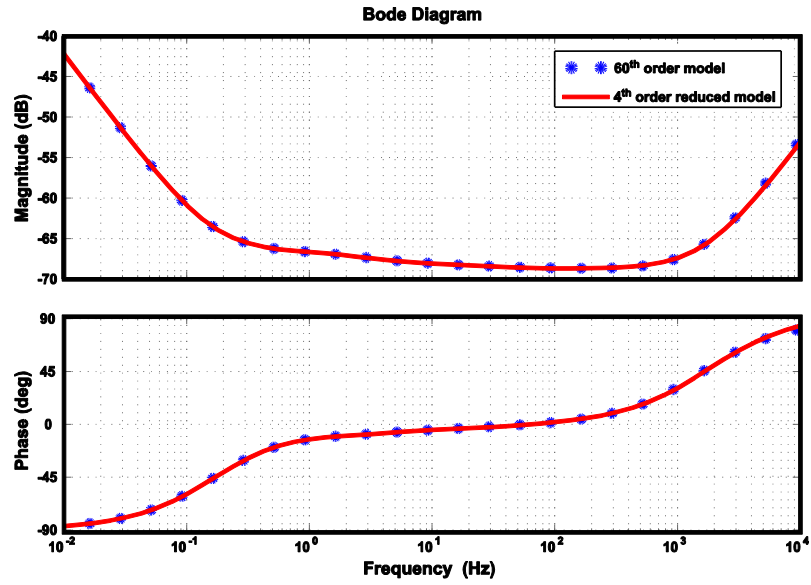


Figure 4.5 Frequency response of the supercapacitor impedance in 60th and 4th order models extracted by SPA method

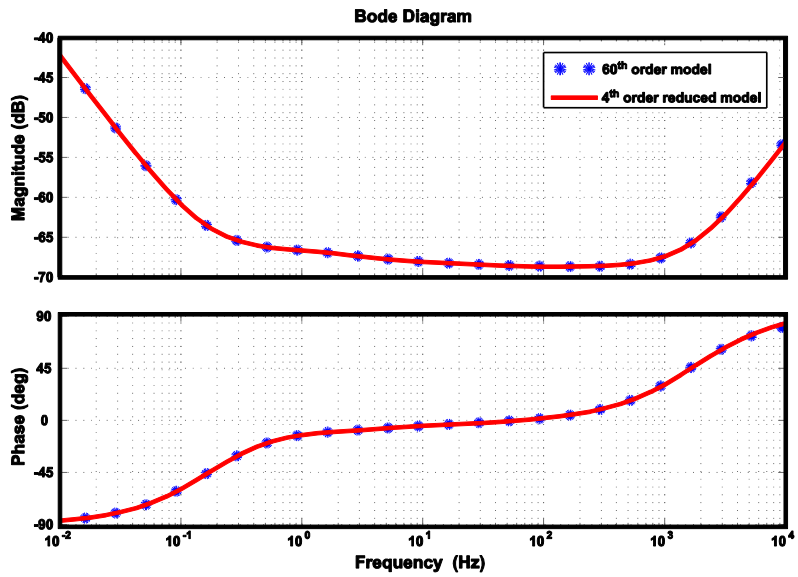


Figure 4.6 Frequency response of the supercapacitor impedance in 60th and 4th order models extracted by TBR method

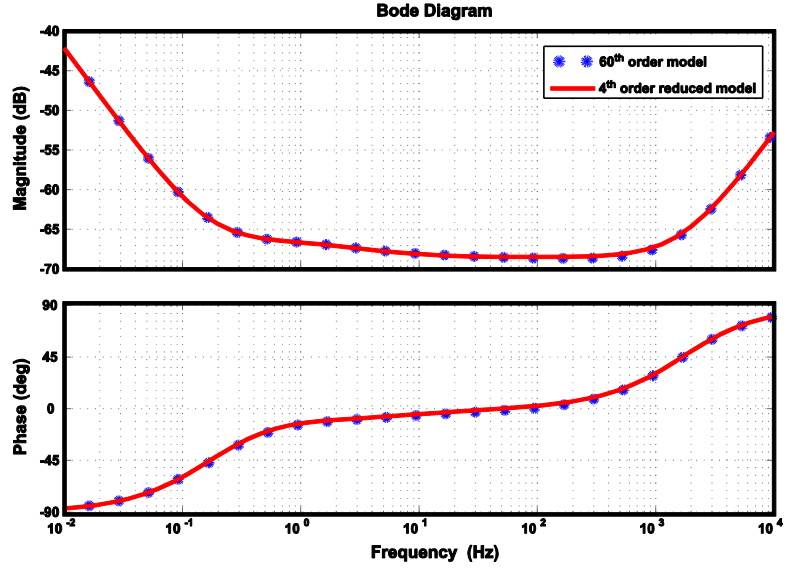


Figure 4.7 Frequency response of the supercapacitor impedance in 60th and 4th order models extracted by Krylov-subspace method

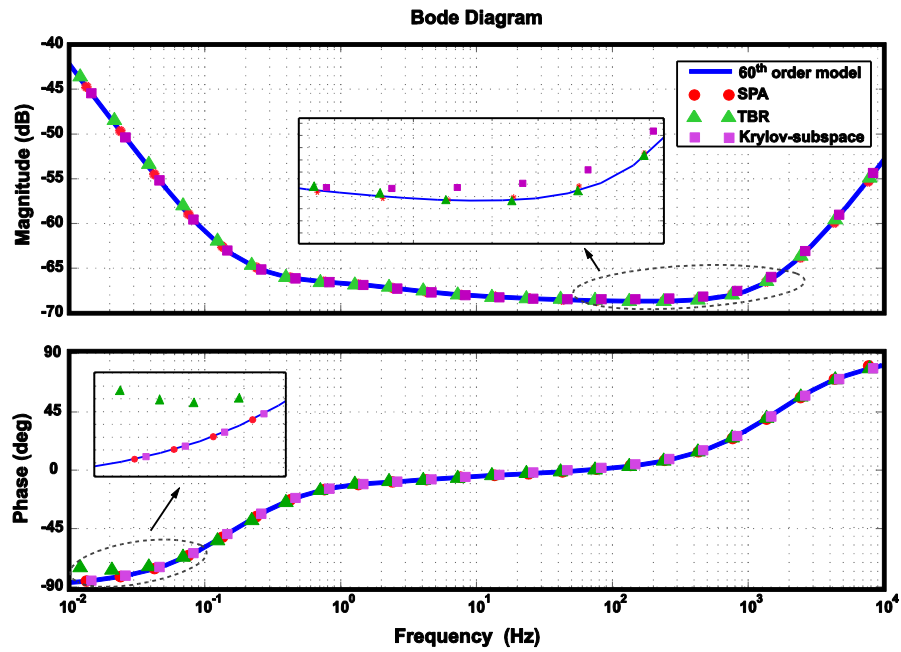


Figure 4.8 Frequency response of the supercapacitor impedance in 60th and 4th order models extracted by: SPA , TBR, and Krylov-subspace methods

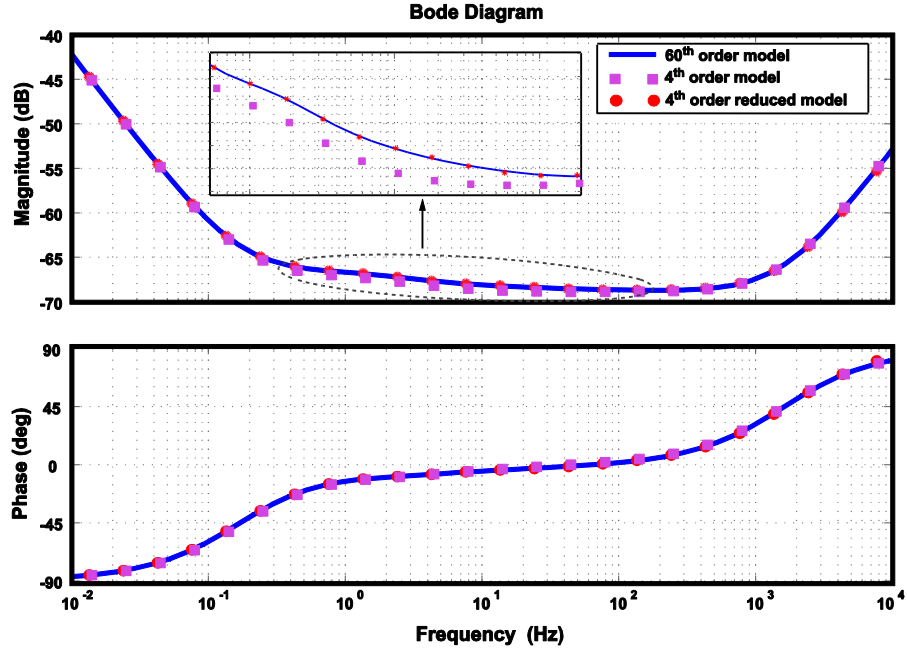


Figure 4.9 Frequency response of the supercapacitor impedance in 60th, 4th models and reduced 4th order model (by SPA method)

In general, order reduction techniques simplify model formulation while preserving simulation accuracy. A high-order RC parallel-branch model (60th order) is first set forth and then 4th order reduced models have been extracted using different numerical reduction techniques. It has been shown that among the reduction techniques used in this thesis, the SPA method is the most precise method for reducing the circuit-based high-order models. The accurate and fast simulation results can be achieved by using the extracted reduced model of the supercapacitor in simulation software tools in order to observe the dynamic behavior of the supercapacitor particularly operated in HEV applications.

CHAPTER 5

ACCELERATED SIMULATION OF SUPERCAPACITOR USING WAVEFORM RELAXATION METHODS

In this chapter, WR method and its implementation in TLM of supercapacitor is discussed. The advantages of WR method is efficiently exploited for TLM of supercapacitors for rapid simulation results. In the following sections, first, parameter identification and validation for the TLM will be introduced. Then, WR techniques are developed based on the characteristics of TLM. Finally, the efficiency of WR applied to TLM is demonstrated by simulating TLM via both WR and conventional methods and simulations results and improvements in speed is reported at the end.

5.1 Waveform Relaxation Theory

Waveform Relaxation (WR) is a family of iterative methods applied at differential equation levels. WR algorithms have been principally implemented in relaxation-based circuit simulators (e.g., RELAX, MOTIS, and SPLICE) to minimize the simulation time of transient response analysis in time domain [64]. WR method was first introduced by Lelarasmee in the early 1980's to improve convergence speed of VLSI circuit simulation [67]. Later, it was used in fast-transient stability analysis of very large electric power systems [68]-[70]. Moreover, it has been used as a solution to 2-D transmission line problems [71]-[74]. The effectiveness of WR methods on fast time-domain simulation of power electronic systems has been also studied in [75]. In recent research, the WR method has been efficiently used in modeling multiple coupled transmission lines [76], [77] and also as a solution to the large multi-3D subsystem electromagnetic problems [78]. These decoupled subsystems are then discretized by stiffly stable implicit integration methods (e.g., Backward Euler and Trapezoidal rule) as is usually adopted in the process in the

standard circuit simulators (e.g., SPICE). The set of discretized algebraic-equations corresponding to the subsystem is computed independently until satisfactory convergence is achieved for a given time interval of interest. In case of nonlinear dynamic systems, the Newton-Raphson method is also employed to acquire approximated linear algebraic equations for the associated nonlinear algebraic equations. In the final step, Gaussian elimination is utilized to solve the set of linear algebraic equations [67]. The process is repeated until all differential equations corresponding to the circuit components are solved. Interested readers can find the convergence proof and more detailed information about WR methods in [79]-[82]. As an illustration, Figure 5.1 shows the general circuit simulation procedure based on the Gauss-Jacobi relaxation scheme and Backward Euler integration method.

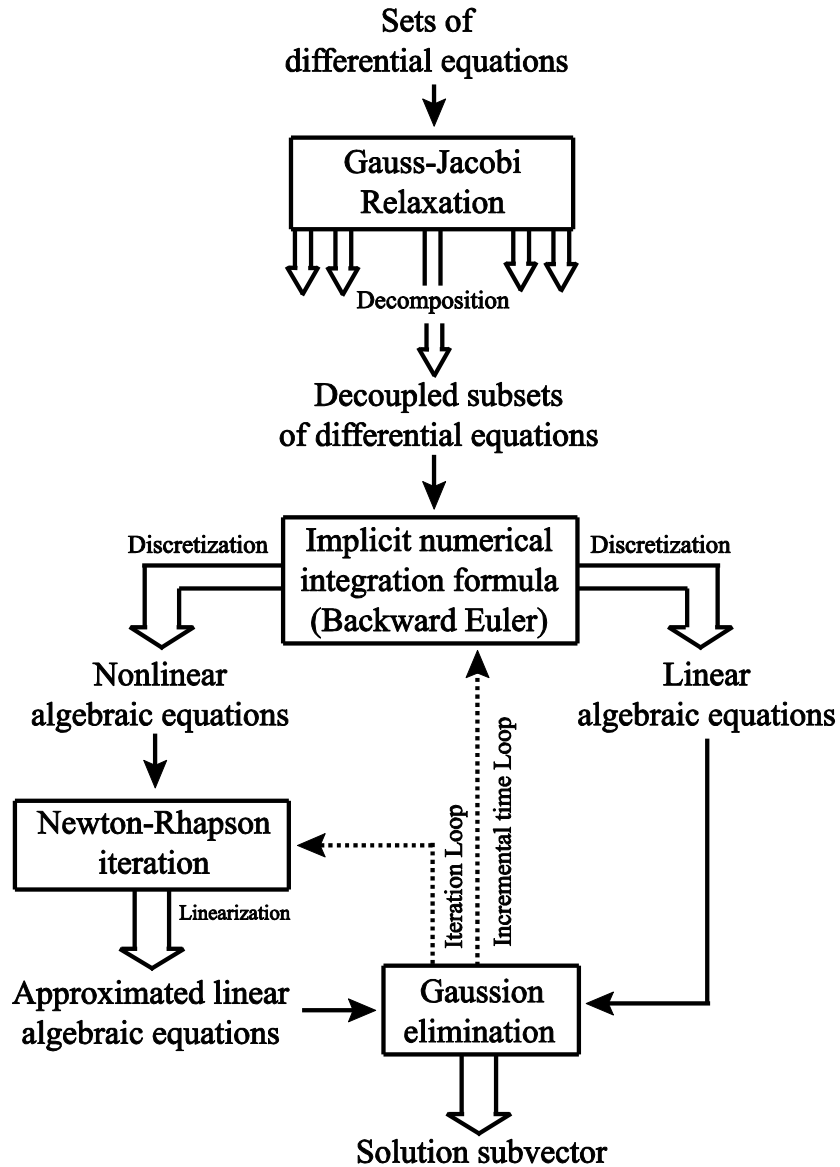


Figure 5.1 Circuit simulation procedure using Gauss-Jacobi waveform relaxation method

In this chapter, the Gauss-Jacobi WR method will be used to decompose the transmission line model (TLM) of supercapacitor into sub-circuits. When the Gauss-Jacobi WR method is applied to TLM of supercapacitor, it acquires faster convergence than conventional methods due to the following advantages of WR over a conventional method.

- In conventional methods, the integration time-step is chosen sufficiently small such that the fastest-changing variable in the circuit can be accurately calculated. The rest of the

circuit variables are forced to be discretized uniformly with the same integration time-step. As a result, the simulation takes longer time due to unnecessary solution points for relatively slow variables. However, each differential equation corresponding to circuit variables can be independently discretized with maximum possible time-step by using WR method. Accordingly, the total number of solution points can be reduced for the state variables displaying slow response in time. In this way, the efficiency of computation can be improved significantly for the systems exhibiting *multirate* (time scale separation) property. The practical use of multirate computation is first introduced by Gear [81], [84] for the circuits equipped with components varying at different rates in the same time interval. Since the TLM has state variables changing at different rates over the same given time interval, this strategy can be easily adopted to reduce the simulation time of TLM. For instance, the variable corresponding to the inductor current in TLM is much faster compared to the other variables, such as capacitor voltages at different nodes. In general, whereas the multirate property yields unnecessary solution points in conventional methods, it can be easily exploited by WR methods to decrease the simulation time [85], [86].

- Another significant advantage of decomposition achieved by relaxation is to exploit *latency* property of the waveform of the sub-circuit variables. The long periods where the value of the variable remains constant is referred as “latency” [87]. By the means of a mechanism detecting the latency behavior of the waveform, this latent period can be bypassed without any computation. In other words, computation only occurs at the time points when a variation in the waveform is observed. It is not possible to exploit this property in the conventional methods since differential equations are solved simultaneously. The latency property is mostly exploited in digital circuits and power systems where the latent periods take place frequently [87]. In case of TLM, the latency has not been exploited due to the continuous small variations at state variables during the transient response.

- Lastly, the convergence of the small algebraic equations describing the behavior of the sub-circuits is much faster than the convergence of the large algebraic equations corresponding to the whole circuit. The reason is that the execution time of the matrix solution of the algebraic equations increases super-linearly with the size of the problem [70]. The speed improvement due to this property can be considerable especially for large integrated circuits [75].

5.2 Analysis of Transmission Line Model (TLM)

The TLM is a widely used equivalent circuit model to accurately simulate the dynamic behavior of supercapacitors due to the properties reported in subsection 3.2.2.1. TLM is also advantageous in WR convergence because of following particular specifications:

- TLM of supercapacitors inherently displays multirate behavior due to very low inductance value and different capacitance values at nodes.
- The circuit variables mostly couple to a small number of other variables, meaning that they are not intensely dependent on one another.
- It is not equipped with any feedback or floating component, which usually causes deceleration in the rate of WR convergence [67].

Considering the aforementioned features, the WR method, if employed, can efficiently ensure rapid convergence of the model. As discussed in Chapter 3, the precision of TLM can be increased by adding as many identical RC branches as possible. However, this leads to the complex analytical expression which is not practical and computationally heavy for simulation. For the sake of simplicity, only a five-stage network with non-identical RC branches, as shown in Figure 5.2, has been used in this study. The parameters of the model are identified from the experimental data, which has been obtained via electrochemical impedance spectroscopy (EIS) as discussed in Chapter 3.

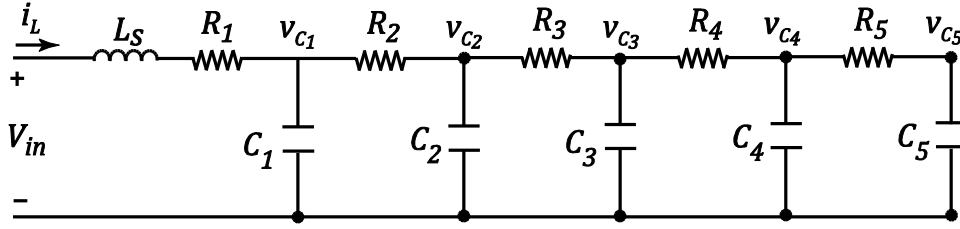


Figure 5.2 Five-stage TLM of supercapacitor

The trial and error method has been used to fit the experimental data into the mathematical expression of the impedance of the network. The impedance of TLM is shown by the following expression:

$$Z(\omega) = j \cdot \omega \cdot L_s + R_1 + \frac{1}{j \cdot \omega \cdot C_1 + \frac{1}{R_2 + \frac{1}{j \cdot \omega \cdot C_2 + \frac{1}{R_3 + \frac{1}{j \cdot \omega \cdot C_3 + \frac{1}{R_4 + \frac{1}{j \cdot \omega \cdot C_4 + \frac{1}{R_5 + \frac{1}{j \cdot \omega \cdot C_5}}}}}}}}} \quad (5.1)$$

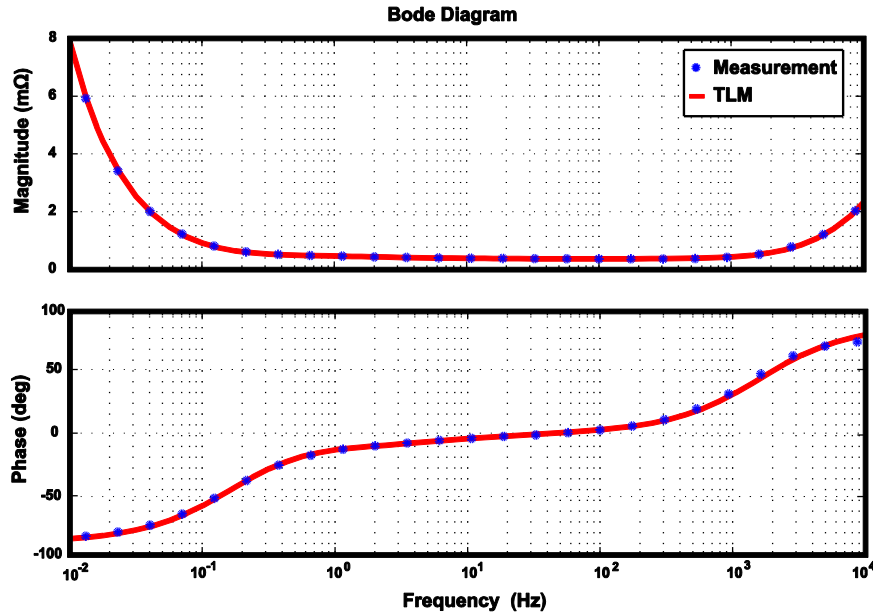


Figure 5.3 Frequency responses of the measured impedance of supercapacitor and the impedance predicted by TLM.

Figure 5.3 shows the perfect match between the measured impedance data and the impedance predicted by the five-stage TLM. In the following sections, the WR method will be applied to this five-stage TLM and the WR techniques will be developed based on the parameter values given in Appendix B.

5.3 Discussion of Waveform Relaxation Techniques

The most widely used techniques in WR, such as circuit partitioning, time windowing and scheduling, will be discussed in this section. These techniques play an important role in the rate of the WR convergence. The idea behind the techniques and their implementation aspects for TLM will be discussed.

5.3.1 Circuit Partitioning and relaxation process

The extracted TLM is divided into smaller sub-circuits by means of the Gauss-Jacobi relaxation scheme, so called circuit partitioning. Circuit partitioning allows the solution of the differential equations corresponding to the sub-circuits with their own maximum possible integration time-step. Despite this advantage, the WR methods may decelerate the speed of simulation if there are any strongly coupled variables solved in different sub-circuits. As studied in [64], these tightly coupled variables must be lumped and the associated differential equations must be computed together with the uniform integration time-step. Moreover, improvement of the rate of WR convergence depends on separating the fast and slow circuit variables accurately in order to integrate with maximum possible integration time-step. Therefore, in circuit partitioning process, one must first determine tightly coupled variables and realize the fast and slow circuit variables in order to have proper circuit partitioning. To do so, the participation factor scheme, which has been used by many researchers as automatic identification of the time responses of dynamic system variables [75], [88], [89] has been used to determine the tightly coupled variables and to realize the fast and slow circuit variables.

The concept of participation factors can be defined over a linear, time invariant system which can be described by state space formulation of the TLM shown in Figure 5.2. The state space description of five-stage TLM is

$$\frac{d\mathbf{x}}{dt} = \mathbf{A}\mathbf{x} + \mathbf{B}\mathbf{u} \quad (5.2)$$

$$y = \mathbf{C}\mathbf{x} + \mathbf{D}u \quad (5.3)$$

where \mathbf{x} is the state vector, \mathbf{A} is the system matrix. u is the system input and \mathbf{B} is the matrix governing the impact of the input on the state variables. For the five-stage TLM model shown in Figure 5.2, the state vector, \mathbf{x} , the input vector, u , and the matrices, \mathbf{A} , \mathbf{B} , \mathbf{C} and \mathbf{D} are

$$\mathbf{x} = [x_1 \ x_2 \ \dots \ x_6]^T = [i_L \ v_{C_1} \ v_{C_2} \ \dots \ v_{C_5}]^T \quad (5.4)$$

$$u = V_{in}, y = i_L \quad (5.5)$$

$$\mathbf{A} = \begin{bmatrix} -R_1/L_S & -1/L_S & 0 & 0 & 0 & 0 \\ 1/C_1 & -1/R_2C_1 & 1/R_2C_1 & 0 & 0 & 0 \\ 0 & 1/C_2R_2 & -(R_2+R_3)/R_2R_3C_2 & 1/R_3C_2 & 0 & 0 \\ 0 & 0 & 1/C_3R_3 & -(R_3+R_4)/R_3R_4C_3 & 1/R_4C_3 & 0 \\ 0 & 0 & 0 & 1/R_4C_4 & -(R_4+R_5)/R_4R_5C_4 & 1/R_5C_4 \\ 0 & 0 & 0 & 0 & 1/R_5C_5 & -1/R_5C_5 \end{bmatrix} \quad (5.6)$$

$$\mathbf{B} = [1/L \ 0 \ 0 \ 0 \ 0 \ 0]^T \quad (5.7)$$

$$\mathbf{C} = [1 \ 0 \ 0 \ 0 \ 0 \ 0] \quad (5.8)$$

$$D = 0 \quad (5.9)$$

The participation matrix indicates the contribution of the state variable on the eigenvalues of the system matrix, \mathbf{A} and can be described by the following expression:

$$\mathbf{P} = [p_{ki}]_{n \times n} = [w_{ki}v_{ki}]_{n \times n} \quad (5.10)$$

where p_{ki} is the participation factor of the k^{th} state variable on the i^{th} eigenvalue and is defined as the multiplication of k^{th} entry of the i^{th} right, v_{ki} and left eigenvectors, w_{ki} of system matrix \mathbf{A} . Assuming \mathbf{v}_i and \mathbf{w}_i are the right and left eigen-vectors corresponding to the i^{th} eigenvalue, λ_i , of \mathbf{A} , the eigen-vectors are normalized as below [75]:

$$\mathbf{w}_i^T \mathbf{v}_i = \begin{cases} 1, & i = j \\ 0, & i \neq j \end{cases} \quad (5.11)$$

The participation factor clearly identifies the contribution of the k^{th} state variables on the i^{th} eigen-value. A state variable can be categorized as a fast (or slow) variable according to its contribution to any fast (or slow) eigen-value. If its participation factor in fast (or slow) eigenvalue relatively contributes more, it can be categorized as a fast (or slow) variable. Moreover, tightly coupled state variables can be identified by their close contribution to the same eigen-values [70].

The participation matrix, \mathbf{P} for the five-stage TLM of the supercapacitor can be found as

$$\begin{array}{c} \lambda_1 \\ \lambda_2 \\ \lambda_3 \\ \lambda_4 \\ \lambda_5 \\ \lambda_6 \end{array} \begin{array}{c} i_L \quad v_{C_1} \quad v_{C_2} \quad v_{C_3} \quad v_{C_4} \quad v_{C_5} \\ \left[\begin{array}{cccccc} 1.0029 & -0.003 & 0 & 0 & 0 & 0 \\ -0.0029 & 0.528 & 0.47 & 0 & 0 & 0 \\ 0 & 0.163 & 0.157 & 0.583 & 0.096 & 0.011 \\ 0 & 0.151 & 0.171 & 0.009 & 0.615 & 0.056 \\ 0 & 0.103 & 0.126 & 0.21 & 0.032 & 0.529 \\ 0 & 0.058 & 0.073 & 0.198 & 0.257 & 0.41 \end{array} \right] \end{array} \quad (5.12)$$

The system matrix of TLM has six different eigenvalues: $\lambda_1 = -10976$, $\lambda_2 = -3593.2$, $\lambda_3 = -238.66$, $\lambda_4 = -31.65$, $\lambda_5 = -99.55$ and $\lambda_6 = -1.288$. The participation matrix indicates that i_L has maximum contribution on the fast eigenvalue, λ_1 , while v_{C_1} and v_{C_2} are more active on the other fast eigenvalue, λ_2 . The rest of the state variables, v_{C_3} , v_{C_4} and v_{C_5} , are more active in the slow eigenvalues, λ_4 , λ_5 and λ_6 , respectively. The participation matrix, \mathbf{P} , implies that $\{v_{C_1}, v_{C_2}\}$ are tightly coupled due to their significant contribution on the mutual eigen-values. However, i_L is decoupled from the rest of the state-variables because it has its only contribution on the fastest eigen-value. Therefore, the first state variable is partitioned node-by-node. The first two and last three voltage nodes are grouped together as intermediate and slow sub-circuits. Figure 5.4 illustrates the partition of the TLM based on the GJ relaxation scheme.

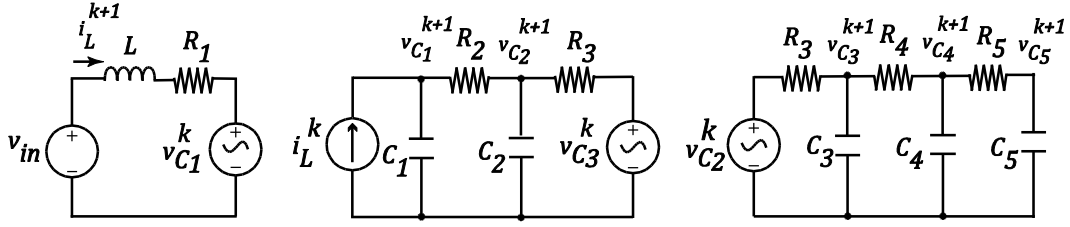


Figure 5.4 Circuit interpretation of GJ-WR applied to the circuit shown in Figure 5.2.

As can be seen from the partition matrix, i_L changes very rapidly compared to the other circuit variables. As already mentioned, the standard simulators using the direct integration methods define the integration time-step to ensure accurate and stable solution of the fastest state variable. An identical time-step is uniformly used to discretize the differential equations corresponding to the slow variables such as v_{C_5} , which results in unnecessary solution points. With the circuit partitioning shown in Figure 5.4, integration time-step of the system of differential equations corresponding to sub-circuits can be determined independently based on the speed of the associated variables. In this way, each sub-circuit of differential equations can be integrated with its own maximum possible time-step, which results in a substantial decrease in solution points.

The resulting decomposed sub-circuits can be expressed by the following equations,

$$\frac{d\mathbf{x}_1^{k+1}}{dt} = \mathbf{f}_1(\mathbf{x}_1^{k+1}, \mathbf{x}_2^k, v_{in}), \quad \mathbf{x}_1(0) = \mathbf{x}_{10} \quad (5.13)$$

$$\frac{d\mathbf{x}_2^{k+1}}{dt} = \mathbf{f}_2(\mathbf{x}_1^k, \mathbf{x}_2^{k+1}, \mathbf{x}_3^k), \quad \mathbf{x}_2(0) = \mathbf{x}_{20} \quad (5.14)$$

$$\frac{d\mathbf{x}_3^{k+1}}{dt} = \mathbf{f}_3(\mathbf{x}_2^k, \mathbf{x}_3^{k+1}), \quad \mathbf{x}_3(0) = \mathbf{x}_{30} \quad (5.15)$$

where, for $i=1,2,3$, $\mathbf{x}_i \in \mathbf{R}^i$ is the subvector of unknown variables allocated to i -th sub-circuit and k denotes the number of iterations. Note that each decoupled sub-circuit is analyzed individually for the entire simulation time interval at each iteration. The previous iterations of decoupled sub-circuits are regarded as decoupling inputs to the sub-circuit currently being

solved. The decoupling inputs are updated at the beginning of the following iteration for each sub-circuit. For example, while solving the differential equation associated with state variable v_{C_1} , the decoupled variable i_L , is treated as input and only updated at the beginning of the next iteration.

After the proper circuit partitioning, any stiffly stable numerical integration scheme can be used to discretize the differential equations of the sub-circuits. For simplicity, the Backward Euler scheme has been applied to each sub-circuit. The relaxation process is also carried out on the set of differential equations corresponding to associated sub-circuits. As an example, the second sub-circuit, which consists of two state variables, $x_2 = v_{C_2}$ and $x_3 = v_{C_3}$, will be investigated. The parameters of matrices **A** and **B** are assumed to be as follows.

$$\mathbf{A} = \begin{bmatrix} a_{11} & a_{12} & 0 & 0 & 0 & 0 \\ a_{21} & a_{22} & a_{23} & 0 & 0 & 0 \\ 0 & a_{32} & a_{33} & a_{34} & 0 & 0 \\ 0 & 0 & a_{43} & a_{44} & a_{45} & 0 \\ 0 & 0 & 0 & a_{54} & a_{55} & a_{56} \\ 0 & 0 & 0 & 0 & a_{65} & a_{66} \end{bmatrix} \quad (5.16)$$

$$\mathbf{B} = [b_1 \ 0 \ 0 \ 0 \ 0 \ 0] \quad (5.17)$$

By recalling the Equation 5.14, the resulting differential equations corresponding to the second sub-circuit is

$$\frac{dx_2^{k+1}}{dt} = a_{21}x_1^k + a_{22}x_2^{k+1} + a_{23}x_3^{k+1} \quad (5.18)$$

$$\frac{dx_3^{k+1}}{dt} = a_{32}x_2^{k+1} + a_{33}x_3^{k+1} + a_{34}x_4^k \quad (5.19)$$

As seen from Equations (5.18) and (5.19), the variables x_1 and x_4 have some coupling effects on the second sub-circuit. These variables are already known values from the most recent previous iteration. Thus, during the computation of the second sub-circuit for the entire given time interval, they are treated as decoupling inputs of the second sub-circuit. If we assume

$$\tilde{\mathbf{u}}_2^k = [a_{21}x_1^k \quad a_{34}x_4^k]^T, \quad (5.20)$$

$$\mathbf{x}_2^{k+1} = [x_2^{k+1} \quad x_3^{k+1}]^T, \text{ and} \quad (5.21)$$

$$\mathbf{A}_2 = \begin{bmatrix} a_{22} & a_{23} \\ a_{32} & a_{33} \end{bmatrix}, \quad (5.22)$$

Equations (5.18) and (5.19) can be reorganized as below

$$\frac{d\mathbf{x}_2^{k+1}}{dt} = \mathbf{A}_2 \mathbf{x}_2^{k+1} + \tilde{\mathbf{u}}_2^k \quad (5.23)$$

where \mathbf{x}_2 is the subvector of unknown variables assigned to the second sub-circuit, \mathbf{A}_2 is the system matrix of the second sub-circuit and $\tilde{\mathbf{u}}_2^k$ is the subvector of decoupling inputs. The differential equations of the second sub-circuit can be discretized by the Backward Euler formula as

$$\mathbf{x}_{n+1} = \mathbf{x}_n + h\mathbf{f}(\mathbf{x}_{n+1}, u(t_{n+1})) \quad (5.24)$$

where h is the step-size and is given by $h = t_{n+1} - t_n$. \mathbf{x}_{n+1} , \mathbf{x}_n are computed values at time t_{n+1} and t_n , respectively. The resulting discretized set of algebraic equations can be expressed as

$$\mathbf{x}_{2,n+1}^{k+1} = \mathbf{x}_{2,n}^{k+1} + h_i(\mathbf{A}_2 \mathbf{x}_{2,n+1}^{k+1} + \tilde{\mathbf{u}}_{2,n+1}^k) \quad (5.25)$$

where h_i is the maximum possible step-size for intermediate sub-circuit (second sub-circuit). If Equation (5.25) is reorganized

$$\mathbf{x}_{2,n+1}^{k+1} = [\mathbf{I} - h_i \mathbf{A}_2]^{-1} (\mathbf{x}_{2,n}^{k+1} + h_i \tilde{\mathbf{u}}_{2,n+1}^k) \quad (5.26)$$

By employing the same procedure, the set of algebraic equations corresponding to the first and third sub-circuits can also be derived as

$$\mathbf{x}_{1,n+1}^{k+1} = [\mathbf{I} - h_f \mathbf{A}_1]^{-1} (\mathbf{x}_{1,n}^{k+1} + h_f \tilde{\mathbf{u}}_{1,n+1}^k + h_f b_1 v_{in}) \quad (5.27)$$

$$\mathbf{x}_{3,n+1}^{k+1} = [\mathbf{I} - h_s \mathbf{A}_3]^{-1} (\mathbf{x}_{3,n}^{k+1} + h_s \tilde{\mathbf{u}}_{3,n+1}^k) \quad (5.28)$$

where h_f and h_s are the assigned time-steps for fast and slow sub-circuits, respectively. The state vectors, system matrices and decoupling inputs are

$$\mathbf{A}_1 = [a_{11}], \quad \mathbf{A}_3 = \begin{bmatrix} a_{44} & a_{45} & 0 \\ a_{54} & a_{55} & a_{56} \\ 0 & a_{65} & a_{66} \end{bmatrix} \quad (5.29)$$

$$\mathbf{x}_1^{k+1} = [x_1^{k+1}], \quad \mathbf{x}_3^{k+1} = [x_4^{k+1} \quad x_5^{k+1} \quad x_6^{k+1}]^T \quad (5.30)$$

$$\tilde{\mathbf{u}}_1^k = [a_{12}x_2^k], \quad \tilde{\mathbf{u}}_3^k = [a_{43}x_3^k \quad 0 \quad 0]^T \quad (5.31)$$

The Equations (5.26), (5.27), and (5.28) are solved for the entire given time interval at each iteration. Iterations are carried out repeatedly until acceptable convergence is achieved. Although the acceptable convergence is achieved with fewer solution points thanks to the optimized time-steps, the iterative property of the WR method has some disadvantages. If the satisfactory accuracy requires much iteration, the convergence rate of WR will decelerate and also storage requirement for the waveforms will increase [67]. However, one can avoid this disadvantage using another technique, so called time-windowing, which will be discussed in the following subsection.

In conclusion, a well-defined circuit partitioning scheme helps to efficiently exploit the multirate behavior of TLM. The basic idea is that all discretized set of algebraic equations are iterated with different step sizes in order to reduce the number of the solution points. One should note that in case of computing the tightly coupled variables in different sub-circuits, the simulation time increases due to the increase in the number of required iterations for satisfactory accuracy [83].

5.3.2 Time Windowing and Scheduling

Another technique used in WR is '*time windowing*'. Whereas the circuit partitioning technique breaks the circuit into sub-circuits based on the characteristics of the variables, the time windowing technique breaks the analysis time of a variable into specific small time intervals describing a part of the whole waveform. As investigated in [75], the iterative solution may give accurate results within a certain time interval, but not outside of that interval. It has also been experimentally observed that partial waveforms require less iteration to achieve certain accuracy

for small time interval. In this way, the number of required iterations can be minimized and, consequently, the convergence rate can be increased substantially. Moreover, time windowing also reduces the storage requirement for the waveforms [90]. This is because the less iterative solutions of partial waveforms require less memory space.

In the literature, several types of time windowing techniques have been proposed: inherent time windowing, dynamic windowing, and fixed and adaptable time windowing [79]. In this thesis, the fixed windowing has been used due to its easy implementation. The size of the fixed window is set to be the step size of the slowest sub-circuit. Figure 5.5 illustrates the simulation process of both WR method and conventional method.

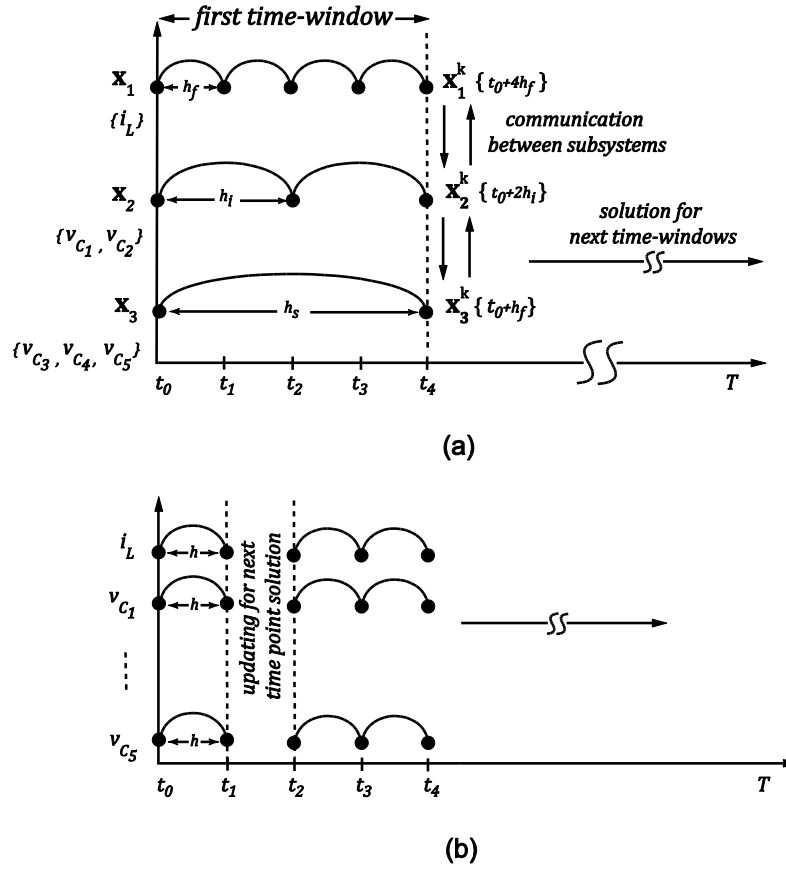


Figure 5.5 The illustration of simulation process of (a) implemented WR method and (b) conventional method.

As seen from the Figure 5.5, the simulation interval $[t_0, T]$ is divided into time windows, $[t_0, t_4]$, $[t_4, t_8]$, $\dots, [t_{4(w-1)}, T]$ in which w is the total number of time windows. It should be noted that

step sizes for sub-circuits are $h_s = 2h_i = 4h_f = t_4$. By choosing a small enough time window, it is ensured that one iteration produces an accurate solution for a time window. At each iteration, each sub-circuit is solved concurrently with its own maximum possible time step for the entire fixed time window. Whereas the conventional method updates the data at each new analysis time point, the WR method only updates the data at the beginning of the next time window. This process is repeated until all variables are converged for the entire simulation interval.

The sequence of the decoupled sub-circuits (or node-by-node decomposed variables) during simulation is another substantial concern affecting the speed of the WR convergence. The process of determining the simulation sequence of the sub-circuits is referred to as *scheduling*. As stated in [79], scheduling becomes strongly effective on the number of iterations whenever Gauss-Seidel relaxation is used in WR. The reason is that the waveforms of decoupled sub-circuits are solved sequentially by using the previously updated waveform for any given iteration. In WR methods based on the GJ relaxation scheme, the waveforms of decoupled sub-circuits are solved concurrently [67], [91]. Therefore, the scheduling has no effect on the speed of the GJ-WR method.

5.4 Experimental Setup and Simulation Results

To verify the accuracy of the extracted TLM of supercapacitor and to prove the efficiency of the WR method in computation time, an experimental setup was conducted as shown in Figure 5.6. The experimental setup is comprised of the supercapacitor (Maxwell Boostcap), a Lecroy 640Zi oscilloscope, a Lecroy voltage probe, a Lecroy CP150 current probe with rated current of 150 Amperes, and a Sorensen DCS40-75E DC power supply, whose rated output voltage and output current are 40 Volts and 75 Amperes, respectively.

The electrical behavior of the supercapacitor during the charging state has been studied by connecting the output terminals of the power supply to the supercapacitor terminals. The current probe was used to measure the current drawn by the supercapacitor and the voltage probe was used to measure the voltage across supercapacitor terminals. The power supply was powered on in standby mode and then the output voltage and current limit of the power supply

were fixed to 2.5 Volts and 70 Amperes, respectively. After a few seconds, the start button was pressed and the data was recorded via oscilloscope.

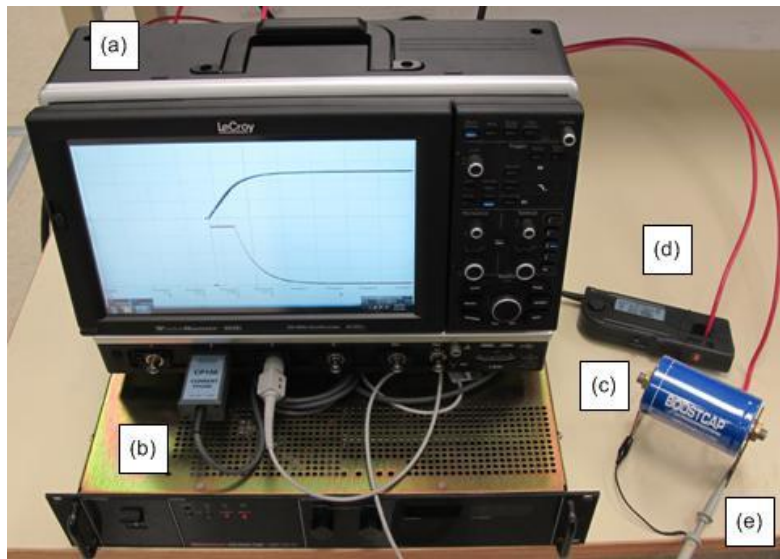


Figure 5.6 The experimental setup: (a) Lecroy 640Zi oscilloscope, (b) Sorensen DCS40-75E DC power supply, (c) supercapacitor (Maxwell Boostcap), (d) Lecroy CP150 current probe, (e) Lecroy voltage probe

The current was first limited to the pre-set value of 70 Amperes by the internal current limitation function of power supply. This is because the initial current would be more than a thousand Amperes if 2.5 Volts was first applied across the terminals of a discharged supercapacitor. In order to avoid this problem, the supercapacitor is first charged with the constant current of 70 Amperes until the voltage at the output terminal of the power supply reaches the preset value of 2.5 Volts. After this time, the operating mode of the power supply changed from constant current to constant voltage. Due to the current flowing through wires from the power supply to the supercapacitor, which have non-zero resistance, the voltage at the terminals of the supercapacitor were less than 2.5 Volts. Thus, the charging process continues with a current less than 70 Amperes, until the voltage at the supercapacitor terminals reaches 2.5 Volts and the current through wires reaches zero. The voltage and the current of the supercapacitor are shown in Figure 5.6.

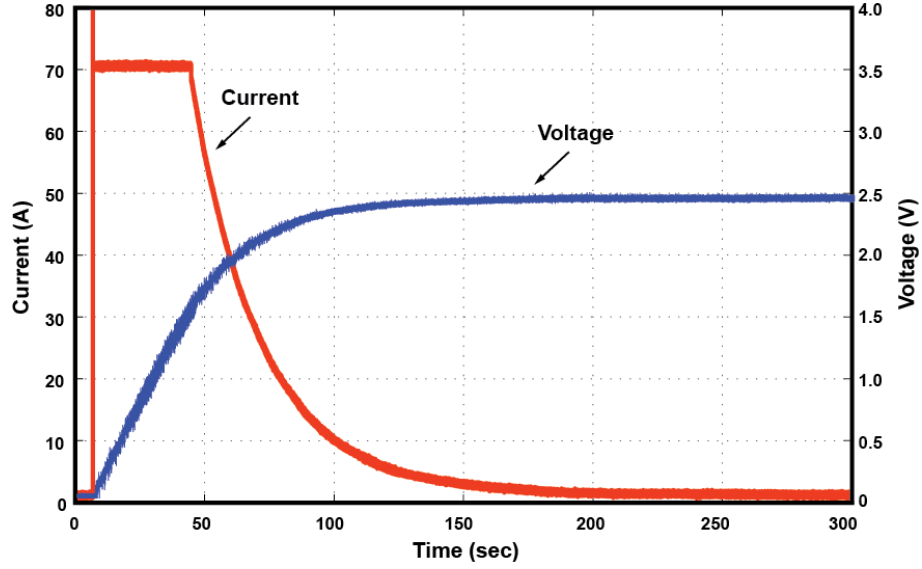


Figure 5.7 The experimental current and voltage measurement

Simulations results for the TLM are presented here to demonstrate the computational advantages of WR techniques discussed previously. The WR method and the conventional method are used to simulate the transient response of input current, i_L . The simulations are carried out using MATLAB/Simulink run on a MacPro[®] computer with dual six-core intel Xeon processor (2.93 GHz) and 64 GB of RAM. To achieve a high level of accuracy, a maximum allowable fixed time-step of 10^{-5} was uniformly used for all unknown variables in the conventional method, whereas the same step-size was only used for the fast sub-circuit in WR method. The decomposition of the TLM allowed the use of different time-steps for each sub-circuit, which decreased the total computation time. The simulation of TLM using conventional method takes 130.2 seconds of CPU time, however, WR convergence only takes 58.3 seconds of CPU time. The comparison between the two methods proves that the convergence speed of WR is roughly 2.5 times faster than the convergence speed of conventional method. Figure 5.8 shows the transient time domain simulation of i_L using conventional fixed-time step method (Backward Euler), and WR method with perfect matching. Note that the voltage data was used as input in simulations. It should be also noted that the simulation of the TLM with identified parameters via EIS analysis almost matches the experimental result.

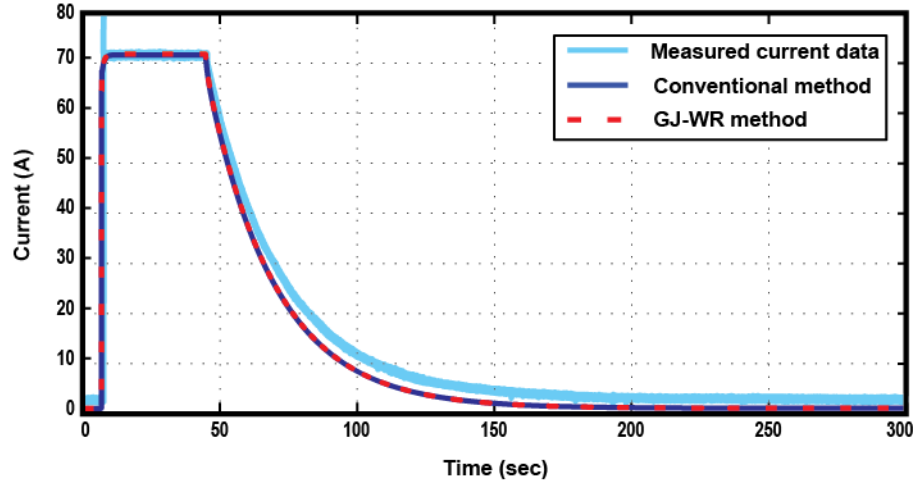


Figure 5.8 Simulation results of the transient response of investigated supercapacitor using WR and conventional methods

In conclusion, fast time-domain simulation of TLM describing the dynamical behavior of supercapacitor has been performed using the WR method. Experimental data obtained by EIS has been used to determine the parameter values for the TLM. Circuit partitioning and time-windowing techniques have been applied to the TLM in order to develop a mathematical model for fast time-domain simulation of supercapacitor. It has been shown that the developed techniques accelerate the convergence speed by about 2.5 times without compromising the simulation accuracy.

CHAPTER 6

CONCLUSIONS

This thesis first investigates the characteristics of supercapacitor by employing the impedance spectrum analysis. Subsequently, parameter identifications and calculations have been conducted for equivalent circuit models of the supercapacitor, namely the RC parallel-branch model and the transmission line model. The frequency responses of the impedance predicted by the extracted circuit models have been compared with the measured impedance data to validate the accuracy. Due to the unique features of these circuit models, such as high accuracy, easy parameter identification, and easy adaptation to the simulation software tools, they can be efficiently utilized in specific simulation tools, e.g., VTB, ADVISOR, and PSAT, to model the dynamic behavior of supercapacitor during designing ESUs for HEVs. However, these models are computationally heavy in simulations due to their higher-order property compared to the other existing equivalent circuit models.

In this thesis, different approaches have been applied to both circuit models to reduce the computation time with acceptable accuracy loss. In the first approach, different numerical order reduction techniques have been utilized to reduce a 60th order RC parallel-branch model to the 4th order model. Among the reduced 4th order models, the reduced model extracted by the SPA reduction technique shows excellent matching with the experimental measurements. Consequently, the accurate and fast simulation results can be achieved by using the reduced 4th order model of the supercapacitor in simulations. In the second approach, the W R method has been used for numerical simulation of TLM of supercapacitor. Circuit partitioning and time windowing techniques have been properly developed to efficiently reduce the computation time. The simulation results show that the rate of WR convergence is approximately 2.5 times faster than the conventional method.

Since the sub-circuits partitioned by GJ relaxation scheme can be solved concurrently, parallel computation can be employed in multi-processor computers to improve the efficiency of the GJ-WR convergence. In this way, the convergence rate of WR method can be improved significantly.

APPENDIX A
SUPERCAPACITOR DATA SHEET

	BCAP2000
Rated capacitance [F]	3,000
Capacitance tolerance [%]	20
Rated voltage [V]	2.7
Maximum voltage [V]	2.85
Maximum ESR _{DC} (25°C) [mΩ]	0.35
Maximum power density [W/kg]	14,000
Maximum peak current [A]	1,600
Specific energy density (2.5 V) [Wh/kg]	5.6
Weight [g]	360
Operating temperature range [°C]	(-40) – (65)
Storage temperature range [°C]	(-40) – (70)
Cycle life	1,000,000
Lifetime (25 °C and 2.7 V)	10 years

APPENDIX B
CIRCUIT PARAMETERS

Parallel RC Ladder Model (60 th ORDER)				
Parameter	L_s	R_e	R_{el}	C_{dl}
Value	36 nH	0.368 m Ω	0.312 m Ω	2050 F

Five-Stage Transmission Line Model						
Parameter	L_s	R1	R2	R3	R4	R5
Value	36 nH	0.396 m Ω	0.004 m Ω	0.032 m Ω	0.04 m Ω	0.08 m Ω
Parameter	C1	C2	C3	C4	C5	
Value	130 F	160 F	380 F	440 F	620 F	

REFERENCES

- [1] D. W. Gao, C. Mi, and A. Emadi, "Modeling and simulation of electric and hybrid vehicles," *Proc. IEEE*, vol. 95, no. 4, pp. 729-745, Apr. 2007.
- [2] H. Behjati and A. Davoudi, "Comparative reliability analysis of hybrid systems for vehicular applications," *Proc. IEEE Transportation Electrification Conf.*, Dearborn, MI, 2007, pp. 791-795, to be published.
- [3] M. E. Glavin and W. G. Hurley, "Ultracapacitor/ battery hybrid for solar energy storage," *Proc. Universities Power Engineering Conf.*, Galway, 2007, pp. 791-795.
- [4] R. A. Dougal, L. Gao, and S. Liu, "Ultracapacitor model with automatic order selection and capacity scaling for dynamic system simulation," *J. Power Sources*, vol. 126, no. 1-2, pp. 250-257, Feb. 2004.
- [5] L. U. Gokdere, K. Benlyazid, R. A. Dougal, E. Santi, and C. W. Brice, "A virtual prototype for a hybrid electric vehicle," *Mechatronics*, vol. 12, no. 4, pp. 575-593, 2002.
- [6] L. Gao, R. A. Dougal, S. Liu, and D. J. Patterson, "Application of virtual test bed in design and testing of hybrid electric vehicles," *J. Power Sources*, vol. 126, pp. 250-257, Feb. 2004.
- [7] T. Wei, X. Qi, and Z. Qi, "An improved ultracapacitor equivalent circuit model for the design of energy storage power systems," in *Proc. ICEMS*, Seoul, 2007, pp. 69-73
- [8] R. C. Kroeze and P.T. Krein, "Electrical battery model for use in dynamic electric vehicle simulations," *Power Electronics Specialists Conf.*, 2008, pp. 1336-1342.
- [9] D. W. Dennis, V. S. Battaglia, and A. Belanger, "Electrochemical modeling of lithium polymer batteries," *J. Power Sources*, vol. 110, no. 2, pp. 310-320, Aug. 2002.

- [10] P. Rong and M. Pedram, "An analytical model for predicting the remaining battery capacity of lithium-ion batteries," *Proc. Design, Automation and Test in Europe Conf. and Exhibition*, 2003, pp. 1148-1149.
- [11] B. Y. Liaw, G. Nagasubramanian, R. G. Jungst, and D. H. Doughty, "Modeling of lithium ion cells-a simple equivalent-circuit model approach," *Solid State Ionics*, vol. 175, no. 1-4, pp. 835-839, Nov. 2004.
- [12] R. L. Sytker and R. M. Nelms, "Classical Equivalent circuit parameters for a double-layer capacitor," *IEEE Trans. Aerosp. and Electron. Syst.*, vol. 36, no. 3, pp. 829-836, Jul. 2000.
- [13] L. Zubieta and R. Bonert, "Characterization of double-layer capacitor for power electronics applications," *IEEE Trans. Ind. Appl.*, vol. 36, no. 1, pp. 199-205, Jan.-Feb. 2000.
- [14] A. Burke, "Ultracapacitors: Why, how and where is the technology," *J. Power Sources*, vol. 91, no. 1, pp. 37-50, Nov. 2000.
- [15] R. Kötz and M. Carlen, "Principles and applications of electrochemical capacitors," *Electrochem. Acta* 45, vol. 45, pp. 2483-2498, Dec. 2000.
- [16] W. Lajnef, J. M. Vinassa, S. Azzopardi, O. Briat, E. Woirgard, C. Zardini, and J.L. Aucouturier, "Ultracapacitors modeling improvement using an experimental characterization based on step and frequency responses," *APEC*, Aachen, 2004, pp.131-134.
- [17] S. Buller, E. Karden, D. Kok, and R.W. De Doncker, "Modeling the dynamical behavior of supercapacitors using impedance spectroscopy," *IEEE Trans. Ind. Appl.*, vol. 38, no. 6, pp. 1622-1626, Nov.-Dec. 2002.
- [18] A. M. Namisnyk, "A survey of electrochemical supercapacitor technology," Bachelor dissertation, Dept. Faculty of Eng., Univ. Sydney, University of Technology, 2003
- [19] S. Atcitty, "Electrochemical capacitor characterization for electric utility applications," PhD. dissertation, Virginia Tech Univ., WV, 2006.

- [20] Youngho Kim. (2003) Ultracapacitor technology powers electronics circuits. Power Electronics Technology.
- [21] S.C. Smith and P.K. Sen, "Ultracapacitors and Energy Storage: Applications in Electrical Power System," *Proc. NAPS*, Calgary, Oct. 2008.
- [22] *EPRI-DOE Handbook of Energy Storage for Transmission and Distribution Applications*, EPRI, Palo Alto, CA, and the U.S. Department of Energy, Washington, DC: 2003. 1001834.
- [23] R. A. Rightmire, "*Electrical energy storage apparatus*," U.S. Patent 3 288 641, Nov., 29, 1966.
- [24] D. L. Boos, "*Electrolytic capacitor having carbon paste electrodes*," U.S. Patent 3 536 963, Oct., 27, 1970.
- [25] J. Motavalli, (2010, December 30), *Start-stop technology: not for hybrids anymore* [Online]. Available: <http://wheels.blogs.nytimes.com>
- [26] D. C. Giancoli, *Physics for Scientists & Engineers with Modern Physics*, 3rd Edition. Prentice Hall: 2000, pp. 719 – 723.
- [27] A. J. Bard and L.R. Faulkner, *Electrochemical Methods: Fundamentals and Applications*. 2nd Ed. John Wiley & Sons, Inc. 2001, pp. 12-13.
- [28] D.C. Grahame: The electrical double layer and the theory of electrocapillarity. *Chem. Rev.* 41, 441, 1947, p. 474.
- [29] B. E. Conway, *Electrochemical Supercapacitors*, 1st Ed. New York, Springer, 1999.
- [30] S. M. Lipka. "The influence of microstructure and carbon content on the performance of electrochemical double-layer capacitors," *Proc. Symp. on Electrochemical Capacitors II*, 1997, p. 153.
- [31] S. Trasatti, P. Kurzweil, *Platinum Met. Rev.* vol. 38, 1994.
- [32] A. Burke, "Ultracapacitors: why, how, and where is the technology," *J. Power sources*, vol. 91, no. 1, pp. 37-50, Aug. 2000.

- [33] A. Schneuwly and R. Gallay, "Properties and applications of supercapacitors: From state-of-the-art to future trends," *Proc. PCIM*, 2000.
- [34] W. Lajnef, J. M. Vinassaa, O. Briata, S. Azzopardia, and E. Woïrgarda, "Characterization methods and modeling of ultracapacitors for use as peak power sources," *J. Power Sources*, vol. 168, no. 2, pp. 553–560, 2007.
- [35] Y. Diab, P. Venet, H. Gualous, and G. Rojat, "Electrical, frequency and thermal measurement and modelling of supercapacitor performance," *3rd European Symp. on Supercapacitor and Appl.*, Rome, 2008.
- [36] F. Rafik, H. Gualous, R. Gallay, A. Crausaz, and A. Berthon, "Frequency, thermal and voltage supercapacitor characterization and modeling," *J. Power Sources*, vol. 165, no. 2, pp. 928-934, Mar. 2007.
- [37] R. de Levie, "On Porous Electrodes in Electrolyte Solutions," *Electrochim. Acta*, vol. 8, no. 10, pp. 751-780, Oct. 1963.
- [38] F. Belhachemi, S. Rael, and B. Davat, "A physical based model of power electric double-layer supercapacitors," *Proc. IEEE-IAS 2000*, Rome, 2000, pp. 3069-3076.
- [39] I. Newton, *Optics*, London, England, 1704.
- [40] B. Taylor, *Methods Incrementorum Directa et Inverse*, London, England, 1715.
- [41] L. Euler, *Institutiones Calculi Differentiatis*. St. Petersburg, Russia, 1755.
- [42] J. L. Lagrange, *Theories des Fonctions Analytiques*. Paris, France, 1759.
- [43] H. Pade, "Sur la representation approchee d'une fonction par des fractions rationnelles," *Philosophy of Doctorate, Math.*, Sorbonne, Paris, France, 1982.
- [44] C. Lanczos, "An iteration method for the solution of the eigenvalue problem of linear differential and integral operators," *Research of the National Bureau of Standards*, vol. 45, no. 4, pp. 255-282, Oct. 1950.
- [45] W. E. Arnoldi, "The principle of minimized iterations in the solution of the matrix eigenvalue problem," *Quarterly J. Appl. Math.*, vol. 9, pp. 17-29, 1951.

- [46] R. Fletcher, "Conjugate gradient methods for indefinite systems," in *Lecture Notes in Math.*, vol. 506, *Numerical Analysis: Proc. Dundee Conf. Numerical Analysis*, 1975, G. A. Watson, Ed. Berlin, Germany: Springer-Verlag, pp. 73-89, 1976.
- [47] Y. Saad and M. H. Schultz, "GMRES: A generalized minimal residual algorithm for solving nonsymmetric linear systems," *SIAM J. Scientific and Statistical Computing*, vol. 7, no. 3, pp. 856-869, Jul. 1986.
- [48] B. C. Moore, "Principal component analysis in linear systems: controllability, observability, and model reduction," *IEEE Trans. Autom. Control*, vol. 26, no. 1, pp. 17-32, Feb. 1981.
- [49] K. Glover, "All optimal Hankel-norm approximations of linear multivariable systems and their L^∞ -error bounds," *Int. J. Control*, vol. 39, no. 6, pp. 1115-1193, 1984.
- [50] L. Sirovich, "Turbulence and the dynamics of coherent structures. Part I: Coherent structures," *Quarterly of Appl. Math.*, vol. 45, no. 3, pp. 561-571, Oct. 1987.
- [51] L. T. pillage and R. A. Rohrer, "Asymptotic waveform evaluation for timing analysis," *IEEE Trans. Comput.-Aided Des. Integr. Circuits Syst.*, vol. 9, no. 4, pp. 352-366, Apr. 1990.
- [52] P. Feldmann and R. W. Freund, "Efficient linear circuit analysis by pade approximation via the Lanczos process," *IEEE Trans. Comput.-Aided Des. Integr. Circuits Syst.*, vol. 14, no. 5, pp.639-649, May. 1995.
- [53] L. M. Silveria, M. Kamon, J. White, L. Miguel, S. Mattan, and K. J. White, "Efficient reduced-order modeling of frequency-dependent coupling inductances associated with 3-D interconnect structures," *32nd ACM/IEEE Design Automation Conf.*, San Francisco, CA, 1995, pp. 376-380.
- [54] A. Davoudi, P. L. Chapman, J. Jatskevich, and A. Khaligh, "Reduced order modeling of high-fidelity magnetic equivalent circuits," *IEEE Trans. Power Electron.*, vol. 24, no. 12, pp. 2847-2855, Dec. 2009.
- [55] A. Davoudi, P. L. Chapman, J. Jatskevich, and H. Behjati, "Reduced-order dynamic modeling of multiple-winding power electronic magnetic components," *IEEE Trans. Power Electron.*, vol.27, no.5, pp. 2220-2226, May. 2012.

- [56] A. Davoudi, P. L. Chapman, and J. Jatskevich, "Nonlinear order reduction in dynamic magnetic equivalent circuits of electromechanic actuators: Incorporating relative motion and back EMF," *Power Electronics Specialists Conf.*, Rhodes, 2008, pp.3992-3995.
- [57] A. Davoudi and P. L. Chapman, "Eddy current modeling with order-reduction in magnetic equivalent circuits," *Power Electronics Specialists Conf.*, Orlando, FL, 2007, pp. 2069-2074.
- [58] F. Cingoz, A. Bidram, and A. Davoudi, "Reduced order, high-fidelity modeling of energy storage units in vehicular power systems," *Vehicle Power and Propulsion Conf.*, Chicago, IL, 2011, pp.1-6.
- [59] Z. Gajic and M. Lelic, "Singular perturbation analysis of system order reduction via system balancing," *Proc. American Control Conf.*, Chicago, IL, 2000, pp. 2420-2424.
- [60] D. M. Vasilyev, "Theoretical and practical aspects of linear and nonlinear model order reduction techniques," Ph.D. dissertation, Massachusetts Inst. Technol., Cambridge, MA, 2008.
- [61] A. C. Antoulas, "Approximation of linear dynamical systems," in *Wiley Encyclopedia of Elect. and Comput. Eng.*, J. G. Webster, Ed. New York, NY: John Wiley, 1998, vol. 11, pp. 403-422.
- [62] R. W. Freund, "Model reduction methods based on Krylov subspaces," *Acta Numerica*, vol. 12, pp. 267-319, Jul. 2003.
- [63] Z. Bai, "Krylov subspace techniques for reduced-order modeling of large-scale dynamical systems," *Appl. Numerical Math.*, vol. 43, no. 1-2, pp. 9-44, Oct. 2002.
- [64] B. N. Bond and L. Daniel, "A piecewise-linear moment-matching approach to parameterized model-order reduction for highly nonlinear systems," *IEEE Trans. Comput.-Aided Des. Integr. Circuits Syst.*, vol. 26, no. 12, pp. 2116-2129, Dec. 2007.
- [65] M. Rewinski and J. White, "A trajectory piece-wise linear approach to model order reduction and fast simulation of nonlinear circuits and micromachined devices," *IEEE Trans. Comput.-Aided Des. Integr. Circuits Syst.*, vol. 22, no. 2, pp. 155-170, Feb. 2003.

- [66] A. Davoudi, "Reduced-order modeling of power electronics components and systems," Ph.D. dissertation, Dept. Elect. and Comput. Eng., Univ. of Illinois at Urbana Champaign, Champaign, IL, 2010.
- [67] E. Lelarasamee, A. E. Ruehli, and A. Sangiovanni-Vincentelli, "The waveform relaxation method for time-domain analysis of large scale integrated circuits," *IEEE Trans. Comput.-Aided Des. Integr. Circuits Syst.*, vol. 1, no. 3, pp. 131-145, Jul. 1982.
- [68] M. I. Spong, M. L. Crow, and M. A. Pai, "Transient stability simulation by waveform relaxation methods," *IEEE Trans. Power Syst.*, vol. 2, no. 4, pp. 943-952, Nov. 1987.
- [69] M. L. Crow and R. Piessens, "The parallel implementation of the waveform relaxation method for transient stability simulations," *IEEE Trans. Power Syst.*, vol. 5, no. 3, pp. 922-932, Aug. 1990.
- [70] M. L. Crow and M. Ilic, "The waveform relaxation algorithm for systems of differential/algebraic equations with power system applications," *American Cont. Conf.*, 1989, pp.1771-1776.
- [71] F. Y. Chang, "The generalized method of characteristics for waveform relaxation analysis of lossy coupled transmission lines," *IEEE Trans. Microw. Theory Tech.*, vol. 37, no. 12, pp. 2028–2038, Dec. 1989.
- [72] F. Y. Chang, "Waveform relaxation analysis of RLCG transmission lines," *IEEE Trans. Circuits Syst. I*, vol. 37, no. 11, pp. 1394–1415, Nov. 1990.
- [73] F. Y. Chang, "Relaxation simulation of transverse electromagnetic wave propagation in coupled transmission lines," *IEEE Trans. Circuits Syst. I*, vol. 38, no. 8, pp. 916–936, Aug. 1991.
- [74] F. Y. Chang, "Waveform relaxation analysis of nonuniform lossy transmission lines characterized with frequency-dependent parameters," *IEEE Trans. Circuits Syst., I*, vol. 38, no. 12, pp. 1484–1500, Dec. 1991.
- [75] J. Sun and H. Grotstollen, "Fast time-domain simulation by waveform relaxation methods," *IEEE Trans. Circuits Syst.*, vol. 44, no. 8, pp. 660–666, Aug. 1997

- [76] N. J. Nakhla, A. E. Ruehli, M. S. Nakhla, and R. Achar, "Simulation of coupled interconnects using waveform relaxation and transverse partitioning," *IEEE Trans. Adv. Packag.*, vol. 29, no. 1, pp. 78–87, Feb. 2006.
- [77] N. J. Nakhla, A. E. Ruehli, M. S. Nakhla, R. Achar, and C. Chen, "Waveform relaxation techniques for simulation of coupled interconnects with frequency-dependent parameters," *IEEE Trans. Adv. Packag.*, vol. 30, no. 2, pp. 257–269, May 2007.
- [78] G. Antonini and A. E. Ruehli, "Waveform relaxation time domain solver for subsystem arrays," *IEEE Trans. Adv. Packag.*, vol. 33, no. 4, pp. 760–768, Nov. 2010.
- [79] J. K. White and A. Sangiovanni-Vincentelli, *Relaxation Techniques for the Simulation of VLSI Circuits*. Boston, MA: Kluwer Academic, 1987.
- [80] A. E. Ruehli and T. A. Johnson, *Circuit Analysis Computing by Waveform Relaxation*. New York, NY: Wiley, 1999.
- [81] Y. L. Jiang, R. M. M. Chen, and O. Wing, "Convergence analysis of waveform relaxation for nonlinear differential-algebraic equations of index one," *IEEE Trans. Circuits Syst.*, vol. 47, no. 11, pp. 1639–1645, Nov. 2000.
- [82] G. D. Gristede, C. A. Zukowski, and A. E. Ruehli, "Convergence properties of waveform relaxation circuit simulation methods," *IEEE Trans. Circuits Syst.*, vol. 45, no. 7, pp. 726–738, Jul. 1998.
- [83] C. W. Gear, "Multirate Methods for ordinary differential equations," Dep. Comput. Eng., Univ. Illinois at Urbana-Champaign, Champaign, IL, 1974.
- [84] C. W. Gear, "Automatic multirate methods for ordinary differential equations," Dept. Comput. Eng., Univ. of Illinois at Urbana-Champaign, Report UIUCDCS-R-80-1000, 1980.
- [85] M. L. Crow and J. G. Chen, "The multirate method for simulation of power system dynamics," *IEEE Trans. Power Syst.*, vol. 9, no. 3, pp. 1684–1690, Aug. 1994.

- [86] R. A. Saleh and A.R Newton, "The exploitation of latency and multirate behavior using nonlinear relaxation for circuit simulation," *IEEE Trans. Comput.-Aided Des. Integr. Circuits Syst.*, vol.8, no.12, pp.1286-1298, Dec. 1989.
- [87] F. A. Moreira and J. R. Marti, "Latency techniques for time-domain power system transients simulation," *IEEE Trans. Power Syst.*, vol. 20, no. 1, pp. 246–253, Feb. 2005.
- [88] I. J. Perez-Arriaga, G. C. Verghese, and F. C. Schweppe, "Selective modal analysis with applications to electric power systems, Parts I: Heuristic Introduction," *IEEE Trans. Power App. Syst.*, vol. PAS-101, no. 9, pp. 3117-3125, Sept. 1982.
- [89] I. J. Perez-Arriaga, G. C. Verghese, and F. C. Schweppe, "Selective modal analysis with applications to electric power systems, Parts II: The dynamic stability problem," *IEEE Trans. Power App. Syst.*, vol. PAS-101, no. 9, pp. 3126-3135, Sept. 1982.
- [90] F. Cingoz, H. Behjati, and A. Davoudi, "Accelerated simulation of ultracapacitors using waveform relaxation method," *Proc. IEEE Transportation Electrification Conf.*, Dearborn, MI, 2012, to be published.
- [91] A. R. Newton, A. L. Sangiovanni-Vincentelli, "Relaxation-Based Electrical Simulation," *IEEE Trans. Comput.-Aided Des. Integr. Circuits Syst.*, vol.3, no.4, pp. 308-331, Oct. 1984.

BIOGRAPHICAL INFORMATION

Fatih Cingoz was born in Bolu, Turkey in 1986. He received his Bachelor's degree in Electrical and Electronics Engineering from Selcuk University in Konya, Turkey in 2008. In the following year, he participated to the Ohio Program of Intensive English (OPIE). He started his Master program in Electrical Engineering at University of Texas at Arlington and has been working as a Master student in Renewable Energy and Vehicular Technology Laboratory since 2010. His current research interest is the modeling and simulation of energy storage devices.